JGR Atmospheres

RESEARCH ARTICLE
10.1029/2021JD035834

Multi-Scale Kelvin-Helmholtz Instability Dynamics Observed by PMC Turbo on 12 July 2018: 2. DNS Modeling of KHI Dynamics and PMC Responses

David C. Fritts[1,2], Ling Wang[1,2], Thomas S. Lund[1,3], S. A. Thorpe[4], C. Bjorn Kjellstrand[5], Bernd Kaifler[6], and Natalie Kaifler[6]

[1]GATS, Boulder, CO, USA, [2]Center for Space and Atmos. Res., Embry-Riddle Aeronautical University, Daytona Beach, FL, USA, [3]University of Colorado, Boulder, CO, USA, [4]School of Ocean Sciences, Bangor University, Menai Bridge, UK, [5]School of Earth and Space Exploration, Arizona State University, Tempe, AZ, USA, [6]Deutsches Zentrum für Luft- und Raumfahrt, Institut für Physik der Atmosphäre, Oberpfaffenhofen, Germany

This article is a companion to Kjellstrand et al. (2022), https://doi.org/10.1029/2021JD036232

Key Points:

- Multi-scale Kelvin-Helmholtz (KH) instability dynamics arise due to natural variations in background flows and initial conditions
- Interacting KH billows induce "tubes" and "knots" that form rapidly and are distinct from secondary instabilities of individual billows
- Tube and knot dynamics evolve more rapidly and yield larger energy dissipation rates than those of individual KH billows

Supporting Information:

Supporting Information may be found in the online version of this article.

Correspondence to:

D. C. Fritts,
dave@gats-inc.com

Citation:

Fritts, D. C., Wang, L., Lund, T. S., Thorpe, S. A., Kjellstrand, C. B., Kaifler, B., & Kaifler, N. (2022). Multi-Scale Kelvin-Helmholtz instability dynamics observed by PMC Turbo on 12 July 2018: 2. DNS modeling of KHI dynamics and PMC responses. *Journal of Geophysical Research: Atmospheres*, *127*, e2021JD035834. https://doi.org/10.1029/2021JD035834

Received 11 SEP 2021
Accepted 9 DEC 2021

Author Contributions:

Conceptualization: David C. Fritts
Formal analysis: David C. Fritts, Ling Wang, Thomas S. Lund, Bernd Kaifler, Natalie Kaifler
Funding acquisition: David C. Fritts

Abstract Kjellstrand et al. (2022), https://10.1029/2021JD036232 describes the evolution and dynamics of a strong, large-scale Kelvin-Helmholtz instability (KHI) event observed in polar mesospheric clouds (PMCs) on 12 July 2018 by high-resolution imagers aboard the PMC Turbulence (PMC Turbo) stratospheric long-duration balloon experiment. The imaging provides evidence of KH billow interactions and instabilities that are strongly influenced by gravity waves at larger scales. Specific features include initially separated regions of KHI, secondary convective and KH instabilities of individual billows, and "tubes" and "knots" that arise where billow cores are mis-aligned or discontinuous along their axes. This study describes a direct numerical simulation of KH billow interactions in a periodic domain seeded with random initial noise that enables excitation of multiple KH billows exhibiting variable phase structures that capture multiple features of the observed KHI dynamics. Variable KH billow phases along their axes yield initial vortex tubes having diagonal alignments that link adjacent, but mis-aligned, billow cores. Weak initial vortex tubes and billow cores having nearly orthogonal alignments amplify, interact strongly, and drive intense vortex knots at these sites. These vortex tube and knot (T&K) dynamics excite "twist waves" that unravel the initial vortex tubes, and drive increasingly strong vortex interactions and a cascade of energy and enstrophy to successively smaller scales in the turbulence inertial range. The implications of T&K dynamics are much more rapid and intense breakdown and decay of the KH billows, and significantly enhanced energy dissipation rates, where these interactions occur.

Plain Language Summary Kelvin-Helmholtz instabilities (KHI) are ubiquitous throughout the atmosphere (and oceans) and have been studied for many years. Interactions between adjacent KH billows seen in early laboratory experiments named "tubes and knots" by Steve Thorpe were only recently recognized in imaging in the mesosphere. These KHI interactions were seen in the laboratory to lead to turbulence faster than secondary instabilities of individual billows. Despite very many papers describing KHI modeling, none have addressed tube and knot dynamics prior to their recent identification in the mesosphere. This paper describes modeling performed to explore the tube and knot dynamics seen during the PMC Turbo experiment and described in the companion paper. Results reveal that tube and knot dynamics yield dramatic increases in energy dissipation that may have important influences in the atmosphere and oceans.

1. Introduction

Atmospheric observations spanning more than six decades have revealed Kelvin-Helmholtz instability (KHI) events ranging in wavelength and depth from very small in the stable boundary layer (SBL) to wavelengths of ∼10 km and larger and depths of a few km in the mesosphere and lower thermosphere (MLT) (see Blumen et al., 2001; Browning & Watkins, 1970; Chapman & Browning, 1997; Chau et al., 2020; Coulman et al., 1995; Eaton et al., 1995; Fritts & Rastogi, 1985; Hecht, 2004; Hysell et al., 2012; James & Browning, 1981; Kelley et al., 2005; Lehmacher et al., 2007; Luce et al., 2002, 2008; Ludlam, 1967; Mesquita et al., 2020; Pfrommer et al., 2009; Scorer, 1951, 1969; Witt, 1962). High-resolution direct numerical simulation (DNS) modeling studies have also confirmed the ubiquity of KHI in multi-scale flows, their implications for signatures in observations,

Investigation: David C. Fritts, C. Bjorn Kjellstrand
Methodology: David C. Fritts, Ling Wang, Thomas S. Lund, C. Bjorn Kjellstrand, Bernd Kaifler, Natalie Kaifler
Project Administration: David C. Fritts
Resources: David C. Fritts
Software: C. Bjorn Kjellstrand
Supervision: David C. Fritts, Thomas S. Lund
Visualization: Ling Wang
Writing – original draft: David C. Fritts
Writing – review & editing: David C. Fritts, S. A. Thorpe

and their potential importance in energy dissipation and mixing from the SBL to very high altitudes (Fritts et al., 2013, 2016; Werne & Fritts, 1999).

KHI influences depend on the spatial scales at which they lead to turbulence and the character and intensities of secondary instabilities (SIs) accounting for their turbulence transitions. These depend, in turn, on internal gravity waves (GWs) that account for the majority of wind shear variance throughout the atmosphere (Balsley & Carter, 1982; Fritts & Alexander, 2003). Generally, GWs having relatively high intrinsic frequencies dissipate via wave breaking at amplitudes approaching convective overturning (Andreassen et al., 1998; Fritts et al., 1998, 2009a, 2009b). Similarly, inertia-GWs having frequencies near the inertial frequency can lead to self-induced KHI (Lelong & Dunkerton, 1998; Thorpe, 1999, 2018). Smaller-amplitude GWs instead modulate such large-scale shears, and thus the scales and intensities of KHI that arise. Additionally, GW superpositions can yield local KHI seen to occur in numerical simulations of multi-scale dynamics (MSD) that appear to account for local KHI events in some observations (Baumgarten & Fritts, 2014, Fritts et al., 2013, 2014; Kjellstrand et al., 2022; hereafter K22).

Individual KHI events alter local environments by mixing momentum, potential temperature, and constituents, thus reducing wind shears and altering tracer gradients where turbulence and mixing is most intense. KHI effects are not only local, however, because they can also play roles in the dissipation of GWs that largely account for energy and momentum transport from lower atmosphere sources to higher altitudes. GW dissipation via KHI (and other instabilities accompanying GW breaking) causes energy and momentum flux divergence and local body forcing that have influences on atmospheric circulation, structure, and variability from small to global scales. Strong local shears leading to KHI are often defined by GWs that are constrained by GW breaking amplitudes, $|u'/(c-U)| \sim 1$, and horizontal wind shears, $|du'/dz = |mu'| \sim N$, for GW horizontal perturbation velocity u', phase speed c, local mean wind U, intrinsic phase speed $c_i = c - U$, vertical wavenumber $m = 2\pi/\lambda_z$, and local buoyancy frequency N.

Laboratory and atmospheric observations have revealed that various KHI SIs can arise together and co-exist because of multiple SI pathways in uniformly or non-uniformly sheared environments enabling KHI formation. Extensive shears often arise due to mean motions and larger-scale inertia-GWs, as noted above, and can lead to extensive KHI displays (Baumgarten & Fritts, 2014; Hecht et al., 2005; K22; Luce et al., 2008; Thorpe, 2002; Witt, 1962). However, a majority of KHI observations suggest significant smaller-scale GW modulations of the underlying shears or localized KHI events from the SBL into the MLT (Eaton et al., 1995; Fritts et al., 2014; Hecht et al., 2014, 2021, hereafter H21; Lehmacher et al., 2007; Pfrommer et al., 2009).

Both GW and KH instability dynamics require a sufficiently large Reynolds number, Re, to exhibit instabilities leading to turbulence. KHI dynamics also require a Richardson number, $\mathrm{Ri} = N^2/(dU/dz)^2$, for buoyancy frequency, N, and assumed planar mean wind, U, sufficiently below 1/4 to enable KHI formation and subsequent SIs leading to turbulence. KHI events having sufficiently low Ri and high Re induce several distinct SI types contributing to turbulence transitions (see Thorpe, 1987, 2002, for reviews of these dynamics). These include the following:

1. Small-scale counter-rotating convective instabilities (CIs) arising within individual KH billow cores and having alignments normal to the billow cores,
2. Small-scale secondary KHI arising in the highly stratified and sheared braids between adjacent billows having varying alignments depending on the KH billow alignments,
3. Billow-scale SIs arising in individual, but non-uniform, KH billows along their axes, such as the billow core undulations described by Fritts et al. (2014, hereafter F14), and
4. Billow-scale or larger SIs referred to as "tubes and knots" arising due to interactions among adjacent or mis-aligned KH billows described by H21 and K22.

The first category, SIs of individual KH billows, were identified in laboratory studies prior to their recognition in the atmosphere (see Thorpe, 1973a, 1973b, 1985, 1987). These include convective rolls arising in the billow cores, and nearer their outer edges for smaller Ri and larger Re (Browand & Winant, 1973; Caulfield et al., 1996; Fritts et al., 2012, 2014; Klaassen & Peltier, 1985, 1989, 1991; Palmer et al., 1994, 1996; Schowalter et al., 1994; Thorpe, 1985; Werne & Fritts, 1999).

The second category, secondary KHI, arise in the stratified braids between adjacent KH billows at somewhat higher Re (Fritts et al., 2012, 2014; Mashayek & Peltier, 2012; Smyth, 2003, 2004). Relative to convective rolls

occurring within the billow cores, secondary KHI appear to contribute less (more) to subsequent KH billow turbulence as Re decreases (increases).

The third category, primary KH billow core undulations induced by non-uniform environments, impose differential core rotation, displacements, and/or distortions that lead to large-scale Kelvin "twist waves" (Kelvin, 1880). These twist waves propagate along the KH billow cores, exhibit instabilities and growth in background shear, and can contribute to KH core unraveling and fragmentation at finite amplitudes (F14). Their dynamics were revealed and analyzed in earlier modeling and analytical studies of GW breaking dynamics (Andreassen et al., 1998; Arendt & Fritts, 1998; Arendt et al., 1997; Fritts et al., 1998, 1999). They were also diagnosed in the transition to turbulence accompanying KHI at sufficient Re (Fritts & Werne, 2000). Importantly, these same dynamics appear to drive the cascade of energy and enstrophy to smaller scales within the turbulence inertial range; hence visualization of twist wave dynamics along or among KH billow cores may provide valuable insights into turbulence dynamics at unobserved smaller scales.

The fourth category, interactions among KH billows where they are closely spaced or mis-aligned, lead to dynamics that were previously identified in the laboratory and the atmosphere (Thorpe, 1987, 2002), but with details and implications only now being explored in detail. Closely spaced KH billows can lead to pairing (Fritts, 1984; Smyth, 2004; Thorpe, 1971, 2002). Mis-aligned billows leading to "tubes" and "knots" (the tubes essentially large-scale versions of secondary KHI) were first revealed in OH airglow imaging over the Andes Lidar Observatory (ALO) in March 2016 (Hecht et al., 2021, hereafter H21). A companion modeling paper (Fritts et al., 2021) was the first to describe the T&K vorticity dynamics that yield strong, larger- and smaller-scale twist waves that drive the cascade to turbulence thereafter. However, Fritts et al. (2021) employed a shear layer having specified variable depth and wind speed (but a uniform minimum Ri) in order to determine the location and character of initial KH billow interactions along their axes, but without the diversity of T&K interactions enabled by random initial noise in this study.

While not recognized in earlier PMC and airglow imaging due to coarser spatial resolution, a review of wide field-of-view (FOV) PMC and OH airglow imaging (~82 and 87 km altitudes, respectively) reveals many examples of apparent KHI exhibiting billow mis-alignments (see Baumgarten & Fritts, 2014; Hannawald et al., 2016; Hecht, 2004; Hecht et al., 2005, 2014; Li et al., 2005; Yue et al., 2010). These suggest that widespread KH billow interactions accompanying modulated shear layers due to underlying small-scale GWs are likely to be very common.

At lower altitudes, observations of KHI revealed in tropospheric clouds spanning ~60 years documented KH billow axial coherence, quantified the typical axial extents of coherent KH billow cores, and anticipated the dynamics contributing to the billow mis-alignments (Ludlam, 1967; Scorer & Wexler, 1963; Thorpe, 2002). Thorpe (2002) also reviewed the evidence for larger-scale influences on KH billow coherence and the scales on which they arise and suggested a typical ratio of KH billow core extent to billow wavelength to be ~3–8.

The spatial scales of KHI increase dramatically from the SBL to the MLT because kinematic viscosity, ν, varies as $1/\rho$, hence increases by $>10^4$ from 0 to ~82 km. For KHI, we specify $\mathrm{Re} = U_0 h/\nu$, where U_0 is half the horizontal velocity difference of the shear layer enabling KHI and h is the half depth of the initial shear layer, as in Werne and Fritts (1999) and multiple other studies. Typically, Re must exceed ~1,000 to exhibit instabilities leading to strong turbulence due to SI types 1 and 2 for an intermediate Ri ~ 0.1 that is roughly consistent with many observations of these KH billow scales and related modeling to date. Importantly, SI types 1 and 2 emerge in KHI that are uniform along their axes at different Re, but with only CIs arising below Re ~ 5,000 for intermediate $0 < \mathrm{Ri} < 0.25$ (Fritts et al., 2014, and other references cited above). Constraints on the occurrence of SI types 3 and 4 at larger Ri and smaller Re have not yet been assessed. However, their significantly larger scales and initiation of earlier and more energetic T&K instability dynamics suggest that they may enable instabilities and turbulence transitions at significantly smaller Re and larger Ri than occur in their absence.

Different Re thresholds imply different minimum KH billow wavelengths, λ_h, that can exhibit SIs and turbulence transitions for given Ri. For these purposes, we assume an approximate relation between KH billow λ_h and a shear layer depth based on theory and modeling of $\lambda_h \sim (4\text{–}5)\pi h$ with $h \sim (\mathrm{ReRi}^{1/2}\nu/N)^{1/2}$. For a minimum Ri = 0.1, maximum shear layer $N_m = 0.028\ \mathrm{s}^{-1}$, $\nu_0 \sim 1.7 \times 10^{-5}\ \mathrm{m}^2/\mathrm{s}$ at Earth's surface, and $\nu \sim 100\nu_0$, $10^4\nu_0$, and $4 \times 10^4\nu_0$ at ~30, 60, and 82 km, the smallest KH λ_h expected to yield strong turbulence due to secondary KHIs (for Re ~ 5,000) are ~4, 40, 400, and 1000 m, respectively, at altitudes of 0, 30, 60, and 82 km. The threshold λ_h at 82 km is smaller than that observed by K22 by a factor of ~5; it is thus consistent with their inference of a range of

Table 1
Acronyms and Abbreviations

ALO	Andes lidar observatory
CI	convective instability
DNS	direct numerical simulation
FOV	field of view
FWHM	full width-half maximum
GW	gravity wave
KH(I)	Kelvin-Helmholtz (instability)
MLT	mesosphere and lower thermosphere
MSD	multi-scale dynamics
PDF	probability density function
PMC	polar mesospheric cloud
Re	Reynolds number
Ri	Richardson number
SAM	Spectral Atmosphere Model
SBL	stable boundary layer
SI	secondary instability
T&K	tube and knot
2-D	two-dimensional
3-D	three-dimensional
F14	Fritts et al. (2014)
H21	Hecht et al. (2021)
K22	Kjellstrand et al. (2022)

secondary instability types expected to arise for the observed KHI $\lambda_h \sim 5$ km, even in a dynamically active environment expected to include pre-existing turbulence that would have reduced the effective Re to some degree. See Table 1 for a list of acronyms and abbreviations employed in our discussion.

Our focus in this paper is on the fourth SI category: those due to interacting KH billows having small Ri and large Re, as suggested by the observations by K22. Of particular interest here are the dynamics of tubes and knots that link adjacent or mis-aligned billows, their competition with individual billow SIs, and their potential to accelerate the breakdown of interacting billows. The model employed for this study, its initial and boundary conditions, and the methods employed to visualize the resulting two- and three-dimensional (2-D and 3-D) fields, are described in Section 2. PMC images revealing the dynamics of interest described by K22 are reviewed in Section 3. Section 4 describes the results of our modeling efforts addressing the dynamics observed by K22, including the initiation and dynamics of tubes and knots, and the relative importance of secondary CIs and KHIs in their absence. Synthetic PMC images computed from the modeling results for comparisons with the observed features are presented in Section 5. A discussion of these results relative to previous analyses and our conclusions are presented in Sections 6 and 7.

2. Fourier Spectral Model

2.1. Spectral Model Formulation and Solution Method

The Spectral Atmosphere Model (SAM) is used for a high-resolution simulation of multiple, interacting KH billows in a domain that allows varying phases and wavelengths along their axes and regions where they are mis-aligned as they arise. The model formulation, solution method, boundary and initial conditions, and analysis and visualization methods are described below. SAM solves the Boussinesq Navier-Stokes equations written in strong conservation law (divergence) form as follows

$$\partial u_j/\partial x_j = 0 \tag{1}$$

$$\partial u_i/\partial t + \partial\left(u_i u_j\right)/\partial x_j = -\left(1/\rho_0\right)\partial p'/\partial x_i + \left(\theta'/\theta_0\right) g\delta_{i3} + \nu\partial^2 u_i/\partial x_j\partial x_j \tag{2}$$

and

$$\partial\theta/\partial t + \partial\left(\theta u_j\right)/\partial x_j = \kappa\partial^2\theta/\partial x_j\partial x_j \tag{3}$$

where (u_i, u_j, u_k) are velocity components along (x, y, z), p, ρ, and θ are pressure, density, and potential temperature (and $\theta = T$ for a Boussinesq fluid), ν and κ are kinematic viscosity and thermal conductivity, primes and "0" subscripts denote perturbation and mean quantities, and successive indices imply summation. These equations specifically enable solutions that are non-hydrostatic.

The Patterson and Orszag (1971) pseudo-spectral algorithm is used to compute the nonlinear products and removal of aliasing errors employs the 2/3^{rds} truncation rule. A low-storage third-order Runge-Kutta method (Williamson, 1980) is used to perform time advancement. The code is highly optimized for massively parallel computers, and we use up to 3,240 cores in this study.

2.2. Boundary and Initial Conditions, Dynamic Large-Eddy Simulation, and Domain

SAM is triply periodic and has initial streamwise (along x) velocity and stability profiles given by

$$U(y,z) = U_0\cos(\pi z/Z)\tanh(z/h) \tag{4}$$

and

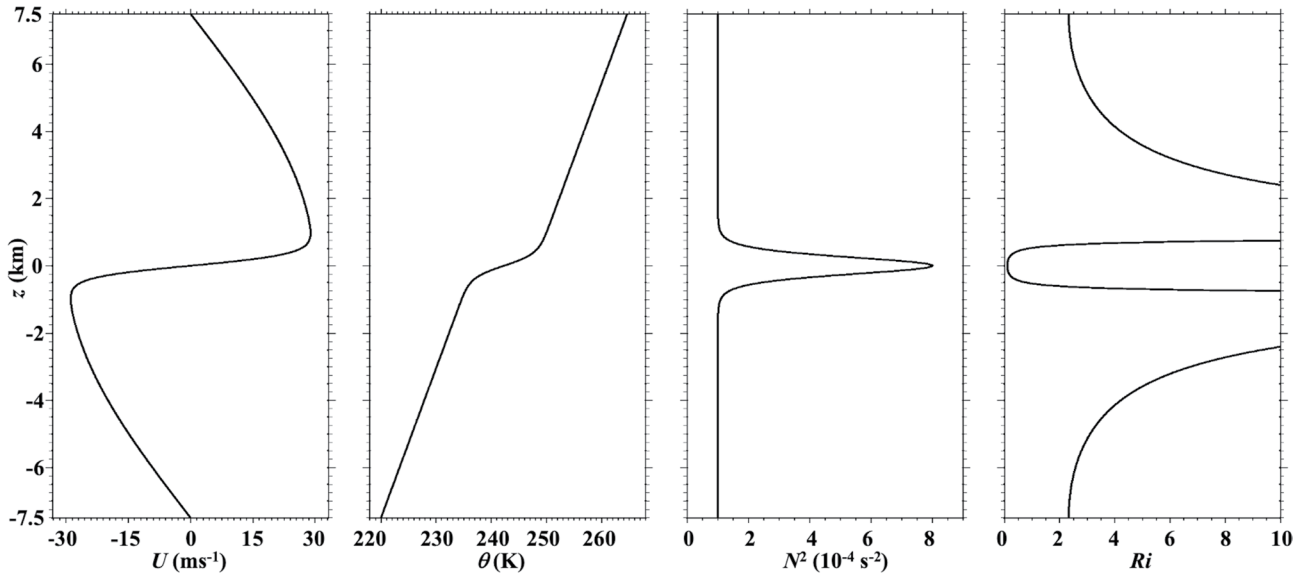

Figure 1. Initial Spectral Atmosphere Model profiles for (left to right) U, θ, N^2, and Ri.

$$N^2(z) = N_0{}^2 + \left(N_m{}^2 - N_0{}^2\right) \operatorname{sech}^2\left[(z - z_0)/h\right] \tag{5}$$

where $U_0 = 31.25$ m/s, $h = 350$ m, $z = 0$ at the domain center, $N_0{}^2 = 10^{-4}$ s^{-2}, and $N_m{}^2 = 8 \times 10^{-4}$ s^{-2} (see Figure 1), implying an initial buoyancy period $T_b = 222$ s at $z = 0$. The domain has dimensions $(X, Y, Z) = (15, 45, 15)$ km so as to allow either 3 or 4 KH billows (denoted wavenumbers $l = 3$ and 4) to arise in the streamwise direction.

The assumed wind profile reflects the need for a strong shear layer in an environment likely having a large-scale, inertia-GW component, given the large horizontal extent of the KHI display described by K22 (this also allows periodicity in the SAM vertical domain). The N^2 profile reflects the expectation that KHI inevitably occurs at a maximum, rather than a minimum, of the background stability in general multi-scale environments (see Fritts et al., 2013).

The wind shear depth and streamwise domain extent allow 3 or 4 KH billows in the 15-km streamwise domain, and variable phase (ϕ) along y (spanwise) that exhibit both secondary CIs and KHIs expected for individual billows. They also induce tubes and knots where variable KH billow phases along y, or mismatched KH billow wavelengths, initiate strong KH billow interactions. The choice to allow 3 or 4 KH billows rather than 1 or 2, or 2 or 3, was made because fewer billows also enabled primary billow pairing, which arises in nature and in MSD including KHI, but which was not prevalent in the PMC Turbo observations described by K22.

These requirements necessitate a larger domain than preferred and very significant computational resources, given our desire to track instability dynamics to the smallest scales employing DNS having isotropic resolution of

$$\Delta x < 1.8\eta \tag{6}$$

for a turbulence Kolmogorov scale, $\eta = (\nu^3/\varepsilon)^{1/4}$ (Moin & Mahesh, 1998; Pope, 2000), for the energy dissipation rate defined as

$$\varepsilon = 2\nu S_{ij} S_{ij} \tag{7}$$

with summation over repeated indices. For these purposes, mean η was assessed on all 2-D model domain planes, and the constraint employed the smallest η on any plane, which is much more strict than typically used because of the very intermittent regions of strong turbulence accompanying initial turbulence transitions in several regions at early times. Resolution of these initial instabilities was judged to be needed to ensure that they had realistic impacts on the larger-scale KH billow and SI evolutions thereafter.

SAM was seeded with non-divergent white noise in velocity with $u_{rms} = U_0 \times 10^{-5}$. The larger scales initiated KHI λ_h having the largest growth rates enabled by the choices for the periodic domain extent and shear depth, thus

$\lambda_h \sim 3.75$–5 km as noted above, but the smaller scales diminished quickly and had weak long-term influences. Because the KHI environment was strongly modulated by small-scale GWs causing additional, intermittent instabilities and turbulence, we anticipated an elevated turbulence background, so also seeded the emerging KH billows with additional white noise with $u_{\rm rms} = U_0 \times 10^{-2}$ when they were well defined, but of small amplitude.

2.3. 3-D Volumetric Visualization and 2-D Imaging

Understanding the complex forms of KHI tubes and knots is enabled by viewing the evolving vortex structures in 3-D volumes. Following earlier studies of the vorticity dynamics arising from GW breaking (Andreassen et al., 1998; Fritts et al., 1998), we employ the negative eigenvalue (λ_2) of the tensor defined as $\boldsymbol{L} = \boldsymbol{\Omega}^2 + \boldsymbol{S}^2$, where $\boldsymbol{\Omega}$ and $\boldsymbol{S}$ are the rotation and strain tensors, with anti-symmetric and symmetric components $\Omega_{\rm ij} = (\partial u_j/\partial x_i - \partial u_i/\partial x_j)/2$ and $S_{\rm ij} = (\partial u_j/\partial x_i + \partial u_i/\partial x_j)/2$, to identify flow features having rotational character (Jeong & Hussain, 1995). λ_2 corresponds to flow features having the greatest rotational, as opposed to shearing, character, and its magnitude is a measure of rotational intensity. Pure shearing motions, in contrast, make no contribution to λ_2. λ_2 thus provides sensitivity to a subset of total vorticity that comprises the majority of the turbulence field (Jeong & Hussain, 1995) and allows us to follow the transition from initial instability structures, through vortex interactions and instabilities, to fully developed turbulence and its subsequent decay.

Implications of KHI T&K dynamics for PMC Turbo imaging were assessed using the method described by F14, which assumed sufficiently short timescales that PMC brightness variations are due only to advection. In this application, a PMC layer having a Gaussian brightness profile, $\beta(z)$, with a full-width/half-maximum (FWHM) of 400 m, based on the lowest, brightest PMC layer seen in the lidar profiling in K22 is assumed. This layer was chosen to be thinner than observed to ensure sensitivity to the diverse dynamical responses. We further assumed that the peak PMC brightness occurred at $z = -300$ m in the undisturbed initial flow, such that KH billow and SI dynamics would be revealed by advection into and around the KH billows in a manner accounting for the major brightness variations seen in the PMC Turbo imaging in K22. This enables sensitivity to SIs due to initial, undisturbed KH billows and arising from T&K dynamics where initial billow cores are mis-aligned or have significant spanwise phase variability. In particular, applications of this method are expected to reveal regions where T&K dynamics and implied mixing result in accelerated KH billow amplitude reductions and reduced or absent axial coherence.

3. KH Billow Instability Dynamics Revealed in PMC Turbo Observations

PMC Turbo imaging revealed multiple KHI events over its ~5.5-day observations, of which that described by K22 was the largest and most dramatic. PMC Turbo imaging during this event was also fortuitously among the brightest throughout the ~5.5-day stratospheric flight. The undisturbed peak PMC brightness extended ~1 km in altitude and comprised a lowest layer having the highest brightness of ~200–300 m FWHM centered at ~82 km, weaker and thinner layers ~200–500 m higher, and a third layer of intermediate brightness at a mean altitude of ~82.9 km (see Figure 2, top). The overall KHI event extended ~100 km horizontally and suggests modulation of the larger-scale shears by a GW having $\lambda_h > 200$ km. Smaller-scale GWs having $\lambda_h \sim 15$ km were also present and appear to have contributed to modulation of the larger-scale shear layer inducing phase and amplitude variability in the KHI response, based on comparable coherence lengths of the KH billows along their axes.

KHI imaging described by K22 exhibits a variety of brightness features that closely resemble those seen in earlier laboratory, modeling, and OH airglow imaging described above. KHI and their SI evolutions spanning 2.5 min seen in PMC Turbo Camera 4 unprojected imaging are shown at 30-s intervals in Figure 2 (bottom). The dominant KH billow λ_h in this event is ~5 km, but it varies somewhat with location and time, likely as a consequence of the significant modulation of the initial shear layer enabling KHI by background GWs having wavelengths of ~15 km and larger.

One region of significant variability exhibiting apparent T&K dynamics is highlighted with black ovals throughout the evolution in Figure 2. The region highlighted at 13:29:30 UT shows two billows (billow cores are dark) at upper left apparently linking to three billows at center right, and an additional interaction below (and further off zenith) that has progressed further by this time. Several bright, narrow, slanted features extending between adjacent billow cores that we interpret as vortex tubes are indicated with red arrows in the images from 13:29:30–13:31 UT. The upper KH billow appears to reconnect thereafter, but those below suggest strong billow dissipation in the region of strong initial interactions by 13:32 UT.

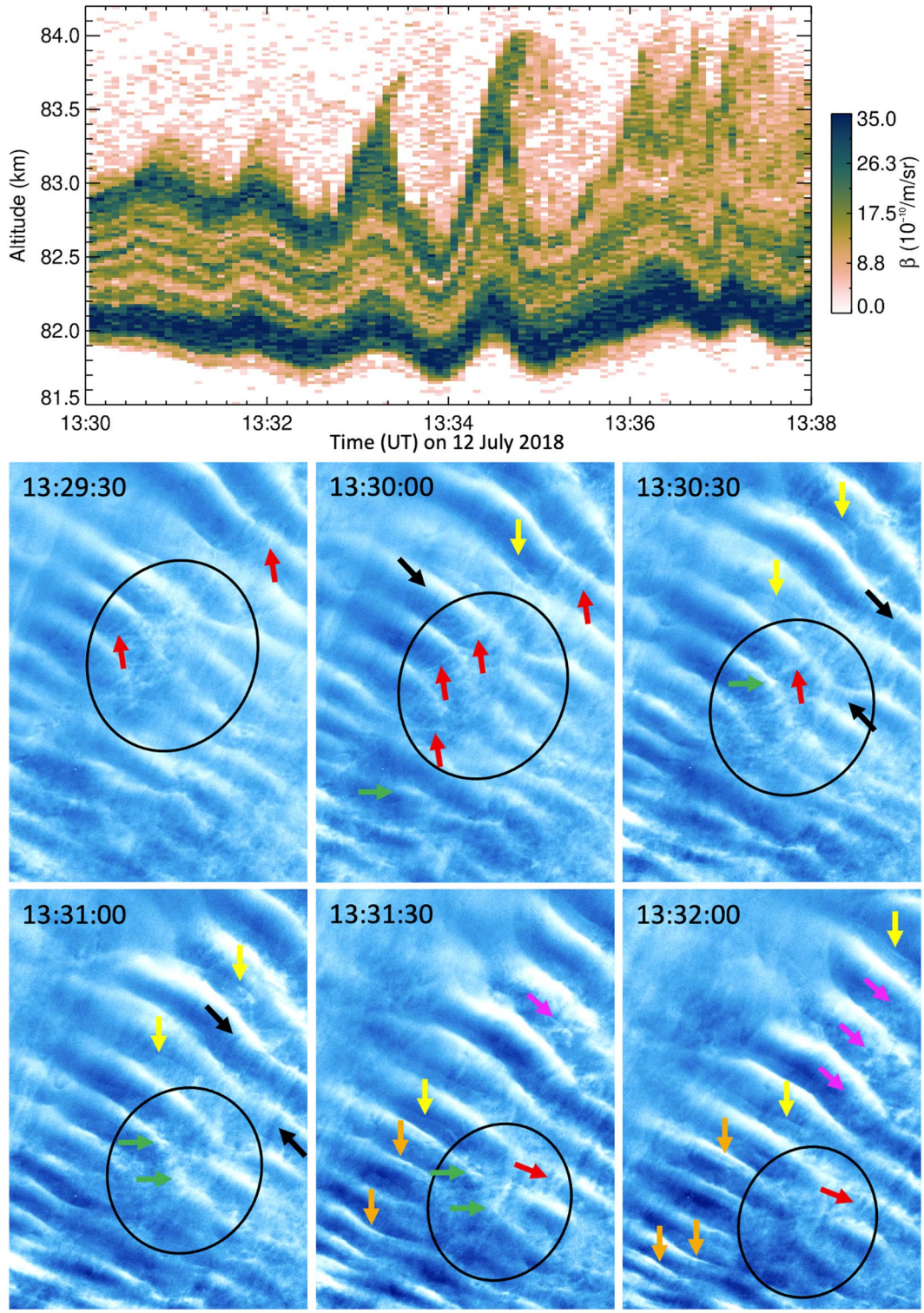

Figure 2. (top) Rayleigh lidar polar mesospheric cloud (PMC) brightness showing Kelvin-Helmholtz (KH) billows ~20 km from the PMC imaging (bottom). Unprojected imaging of Kelvin-Helmholtz instability (KHI) having λ_h ~ 5 km with arrows identifying initial vortex tubes between, over, or under distorted KH billows and arising at later times (red), secondary KHI between, and CI within, KH billows (yellow and black), thin linear dark features where secondary KHI form and are entrained from above (orange), bright emerging knots where vortex tubes overlie or underlie billow cores (green), and small scalloped features (pink). Black ovals track the primary region of tube and knot dynamics. The imaging interval spans ~0.67 T_b.

Also highlighted in Figure 2 are apparent CIs (Category 1 SIs) aligned roughly orthogonal to the KH billows (black arrows), secondary KHI (Category 2 SIs) between adjacent KH billows (yellow arrows), and vortex tubes (Category 4 SIs) arising between adjacent KH billows (red arrows) that initiate T&K dynamics where KH billows are mis-aligned. Additional vortex tubes linking adjacent KH billows also appear adjacent to evolving T&K dynamics. The timing of these SIs suggests that the progression to turbulence and billow core breakdown is most rapid accompanying the evolutions of tubes and knots.

4. Modeled KH Billow Coherence, Tube and Knot Dynamics, and Other SIs

4.1. Influences of Random Initial Conditions on KH Phase and λ_h Variability

We first explored the dependence of KH billow coherence along their axes on very small, random perturbations to an initially uniform unstable shear layer. For this purpose, we performed 10 short simulations having different initial white noise seeds in velocity as described above. The various noise seeds yielded a range of responses having fewer or more examples of KH billow orientations leading to tube and knot dynamics. One of these cases exhibiting both weaker and stronger KHI phase variations along their axes yielding somewhat confined T&K dynamics is shown with horizontal cross sections of $T'/T(x, y)$ and $T/T_0(x, z)$ from 3 to 4.5 T_b at top and bottom in Figure 3.

$T'/T_0(x, y)$ cross sections at top in Figure 3 reveal a superposition of weaker and stronger KH billow phase variations along y, $d\phi/dy > 0$, for increasing ϕ along x, that must be periodic in the SAM code. The larger of these from $y \sim$ 5–25 km exhibit strong perturbations of the $T'/T_0(x, y)$ fields that indicate additional vortex dynamics penetrating the $z = 0$ plane at several sites at 3 and 3.5 T_b. These are seen below to drive accelerated transitions to turbulence in these regions in comparison to the relatively undisturbed region at $y \sim$ 30–45 km. Successive times at top in Figure 3 reveal rapid transitions to smaller scales, less coherent structures at the initial shear layer, and a breakup of the initially coherent KH billows along y as turbulence and mixing arise in the billow cores and stratified braids. The evolution displayed spans only 1.5 T_b, or ∼5.5 min, given the strong initial stratification yielding $T_b = 222$ s at the initial shear layer.

Lower panels in Figure 3 show $T/T_0\,(x, z)$ at the sites centered at the white dashed lines at top left. Those at $y = 13$ and 22 km show examples of KH T&K dynamics; those at $y = 36$ km show KH billow evolutions occurring largely without T&K effects at early times.

The $T/T_0\,(x, z)$ cross section at $y = 36$ km exhibits the most uniform and coherent KH billows because their evolutions occur where $d\phi/dy \sim 0$. They exhibit (a) significant rollup by 3 T_b, (b) very weak SI tendencies by 3.5 T_b, (c) emerging secondary CI and KHI by 4 T_b, and (d) finite-amplitude secondary CI and KHI yielding strong turbulence by 4.5 T_b, but retaining laminar billow cores.

In contrast, the T&K evolutions at $y \sim$ 10–15 and 20–25 km exhibit KH billow deformations seen at 3 T_b to accompany distortions due to initial, larger-scale KH billow dynamics induced by strong, local $d\phi/dy > 0$, especially in the two KH billow cores at smaller x. Both cases include vortex structures penetrating the $z = 0$ plane at $y \sim$ 13 and 22 km at top in Figure 4. These are seen in the $T/T_0\,(x, z)$ cross sections at bottom to have a single vortex penetrating the x-z plane between adjacent KH billow cores at $y = 13$ km and two vortex cores penetrating the x-z plane between adjacent KH billow cores at $y = 22$ km at bottom in Figure 4. In both cases, the associated KH billow(s) are seen in Figure 3 at bottom to exhibit earlier instability dynamics transitions (by 3.5 T_b) and much more fully evolved billow turbulence (by 4 T_b) relative to those at $y = 36$ and 45 km.

Another perspective on this multi-scale KHI evolution is shown with horizontal cross sections of vorticity magnitude, $|\zeta|(x, y)$ at $z = 0$, for $\boldsymbol{\zeta} = \nabla \times \boldsymbol{u}$, at top in Figure 4. The $|\zeta|(x, y)$ field at 3 T_b exhibits several types of responses. KH billow cores have relatively weak, primarily spanwise vorticity, $\zeta_y > 0$, seen largely in colors from light blue to green. Vortex sheets evolving from the initial shear layer wrap around the emerging KH billows at 3 T_b. These are seen where they penetrate the $z = 0$ plane between adjacent billows having enhanced $\zeta_y > 0$ with thin red maxima. The more prominent features in this field at 3 T_b are the swirls seen having clockwise rotation as viewed from above, thus with $\zeta_z < 0$ (vorticity into the image). Because these vortex tubes arise on the initial vortex sheet, they remain within the vortex sheet, thus also have $\zeta_y > 0$ and $\zeta_x < 0$, as will be seen more clearly below. Where vortex tubes arise, the adjacent billow cores also show significantly enhanced vorticity, and these will be seen to be the sites of initial T&K dynamics that drive the most rapid and energetic turbulence evolutions thereafter.

$|\zeta|(x, z)$ cross sections at the y locations shown with dashed white lines at top left in Figure 3 are shown at the same times in the lower panels of Figure 4. These fields largely confirm the discussion of the $T/T_0\,(x, z)$ cross sections at

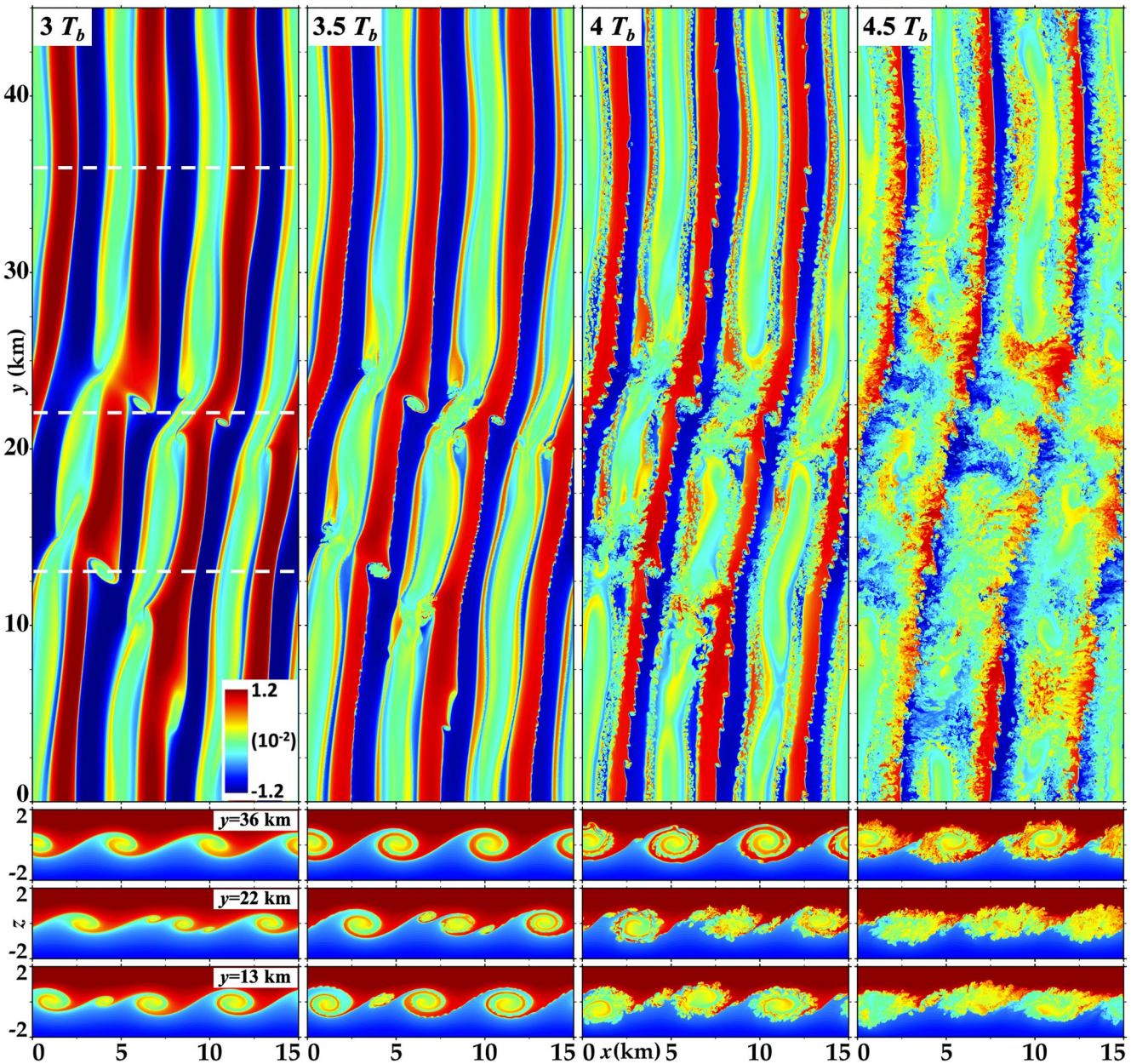

Figure 3. (top) T'/T_0 (x, y) at $z = 0$ and (bottom) T/T_0 (x, z) at $y = 13$, 22, and 36 km (see dashed lines at top left) at 3–4.5 T_b (left to right). The color scale is shown at lower right in the upper left panel.

bottom in Figure 3. However, they more clearly reveal the evolutions from strongly interacting initial vortex tubes and billow cores leading to knots, and the emerging strong turbulence driven by these dynamics.

4.2. KHI T&K Dynamics Seen in 3-D Imaging

To better understand the T&K dynamics driving turbulence transitions and increasing intensities revealed in the T'/T_0 and $|\zeta|$ fields discussed above, we employ 3-D imaging of λ_2 for the two strongest events occurring at ~8–16 km at smaller x and at ~18–24 km in the domain center shown with yellow rectangles at top left in Figure 4 labeled 1 and 2 (Regions 1 and 2). These show T&K dynamics involving (a) one vortex tube linking to two adjacent KH billow cores, and (b) two closely spaced vortex tubes linking to opposite edges of one KH billow core, respectively. The λ_2 evolutions in each case extend from 2.75 to 4 T_b, thus from the laminar initial vortex dynamics driving the turbulence transitions to strong local turbulence that does not yet span a KH billow λ_h.

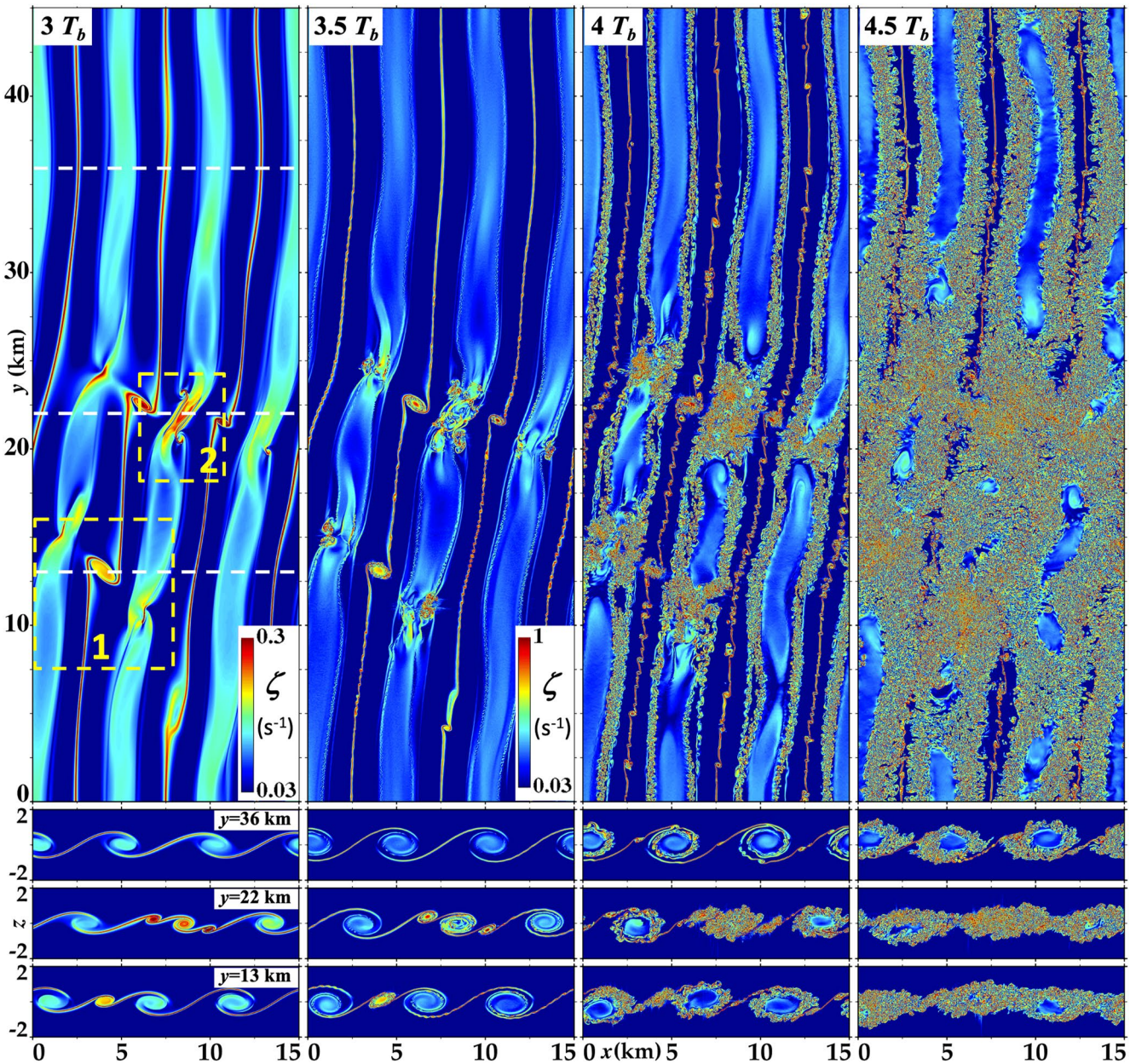

Figure 4. As in Figure 3 showing $|\zeta|(x, y)$ and $|\zeta|(x, z)$ cross sections at the same locations at top and bottom, respectively. The color scales at bottom right are for the first and last three times, respectively, using a log scale. Dashed yellow rectangles show Regions 1 and 2.

T&K dynamics in Regions 1 and 2 exhibit various types of vortex interactions that appear to be universal among all of the various T&K events initiated by our random DNS initial noise field. The drivers of all subsequent dynamics are the interactions among an initial vortex tube and an initial KH billow having a common $\zeta_y > 0$ where they arise in close proximity and entwine due to their mutual advection.

4.2.1. One Vortex Tube Linking Two KH Billow Cores

Region 1 contains two such sites at which vortex T&K dynamics arise, at top where a vortex core emerges on the intermediate vortex sheet underlying the KH billow core at upper left and overlying the billow core at lower right (see the white and yellow arrows at 2.75 T_b in Figure 5). Because both components at each site have $\zeta_y > 0$, they wrap around each other, causing them to become increasingly entwined with increasing proximity and approximately orthogonal alignments, yielding vortex knots (see the green arrows at 3 and 3.2 T_b). The knot regions are initially small, ~1 km in diameter, and host strong and intensifying, but initially laminar vortex interactions.

These accelerate as the vortices wrap increasingly closely, resulting in transitions to strong turbulence that require only ~0.3 T_b and the vortex knots expanding to ~2–3 km by 4 T_b.

The major driver of knot evolutions is differential advection along the axis of each vortex induced by the other. These dynamics excite Kelvin (1880) vortex waves, or "twist waves" that propagate along each vortex tube thereafter (Arendt & Fritts, 1998; Arendt et al., 1997; Fritts et al., 1998; see the blue arrows at 3.4 and 3.5 T_b). Where they arise with large amplitudes, they unravel and fragment the initial vortex tubes. The major contributors to vortex fragmentation are "mode 2" twist waves that essentially un-ravel the initial vortex core, which will be seen more clearly in the discussion of the T&K dynamics occurring in Region 2 below.

The initial vortex tube in Region 1 also entrains the vortex sheet on which it arose and intensifies the smaller, secondary KHI evolving on it (red arrows). The same dynamics at successively smaller scales drive the late stages of the vortex knots (green arrows). Similar dynamics also arise on the intensifying intermediate vortex sheets (see the zoomed view of the white rectangle between adjacent KH billows shown with enhanced color and opacity scales at lower right). These dynamics are smaller-scale versions (by ~10–20 times) of the initial T&K dynamics (pink and orange arrows), but only arise and contribute to turbulence for initial flows having large Re.

4.2.2. Two Vortex Tubes Linking to One KH Billow Core

The Region 2 evolution shown in Figure 6 also exhibits two sites at which initial vortex tubes (white arrows) and a KH billow core (yellow arrow) having $\zeta_y > 0$ are in close proximity. In this case, however, two vortex tubes that are closely spaced in y arising on the vortex sheets upstream (downstream) overlie (underlie) the central billow core. As above, each emerging knot (green arrows) extends over ~1 km at this stage. Co-rotation of the two tubes above and below the billow core induce strong stretching of the billow core between them that did not occur in Region 1. This induces more rapid, stronger, and larger-scale twist waves (blue arrows) than occurs in Region 1 (see the structures in the billow core and the large-scale spirals at the vortex tube "ends" at 3.2 T_b), at which time no such features are seen in the T&K dynamics in Region 1 shown in Figure 5.

Initial, large-scale twist waves excited on the billow core in Region 2 by 3.2 T_b cause its rapid breakdown by ~3.4 T_b, after which only weak, small-scale twist waves are seen. Smaller-scale, more intense twist waves seen emerging on the vortex tube ends in the initial knot regions at 3.2 T_b are seen to exhibit spiral structures that are mode-2 twist wave responses to these knot dynamics (outer blue arrows). They intensify rapidly and essentially unravel the vortex tubes as they propagate away from the initial knot sites (see the disappearing vortex cores accompanying twist wave propagation from 3.2 to 3.8 T_b).

4.2.3. Dynamics of Transitions to Smaller Scales

Seen in Regions 1 and 2 is evidence of the dynamics driving the transition to smaller scales and ultimately what is best characterized as fully developed, sheared and stratified, turbulence. Like the larger-scale T&K dynamics evolutions discussed above, the subsequent evolutions at smaller scales are deterministic processes at each location and time in our DNS, but it becomes impossible to follow the details as the range of spatial scales expands and the dynamics time scales contract.

In the regions of initial T&K dynamics where twist wave generation and vortex fragmentation result in many vortex structures in close proximity, "nearest-neighbor" vortices lead to the same vortex alignments initiating the T&K dynamics. Specifically, see the emergence of smaller-scale twist waves in the knot regions (blue arrows in Figure 5 and outer blue arrows in Figure 6) that intensify, interact, and lead to smaller-scale vortices and increasing complexity beginning ~3.2 T_b. These occur at successively smaller spatial and temporal scales until constrained by viscosity at small local Re. Similar dynamics, but at much smaller scales, arise on the intensifying vortex sheets entrained around the vortex tubes as they intensify in Regions 1 and 2 (see the red arrows in Figures 5 and 6). These emerge as very-small-scale secondary KHI beginning ~3.3 T_b, they intensify due to vortex tube rotation and stretching and wrapping of the vortex sheet, and they ultimately also exhibit strong, small-scale vortex interactions seen emerging at scales of ~100 m and smaller (see the very fine vortex structures highlighted with red arrows, especially from 3.4 to 3.8 T_b in Figure 6).

4.3. KHI Secondary CI and KHI in the Absence of T&K Dynamics

PMC imaging shown in Figure 2 reveals relatively uniform KH billows having expected SIs away from regions of T&K dynamics driving more rapid turbulence transitions. A similar tendency is seen in our DNS results, where

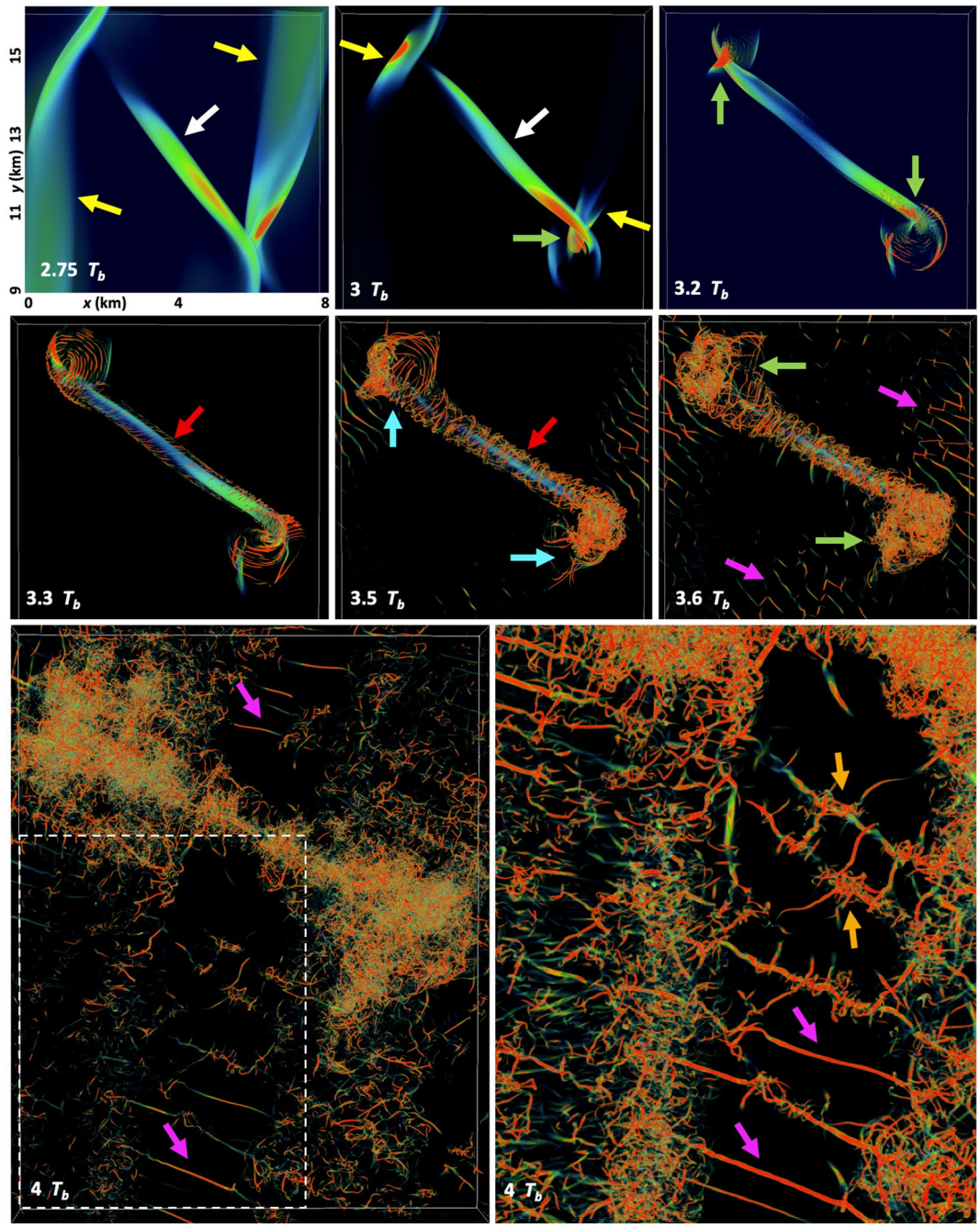

Figure 5. λ_2 (x, y) viewed from above in Region 1 of Figure 4. The λ_2 color (opacity) scale varies from blue to red (transparent to opaque), corresponding to very weak to strong local rotation. λ_2 varies greatly in space and time, has no units, and varies in time to allow optimal definition of larger- and smaller-scale dynamics throughout each event. Vortex elements identified by colored arrows in this case include the initial vortex tube (white), the adjacent billow cores (yellow), emerging and intensifying vortex knots (green), thin vortex sheaths due to entrainment of the initial vortex sheet around the vortex tube (red), secondary KHI and vortex tubes on the initial vortex sheet (pink), and secondary tube and knot dynamics among the secondary KHI and orthogonal vortex tubes (orange). The smaller-scale dynamics in the white rectangle at 4 T_b are shown with enhanced color and opacity scales at lower right.

the initial KHI field has $d\phi/dy \sim 0$ at $y \sim$ 35–40 km, enabling the KHI dynamics in that region to arise largely without influences of T&K dynamics at early stages of the evolution. The T'/T, T/T_0, and $|\zeta|$ fields in Figures 3 and 4 confirm that the absence of T&K dynamics enabled the KH billow evolution in this region to proceed without exhibiting a transition to turbulence up to ~4 T_b, thus delaying turbulence onset by ~0.7 T_b.

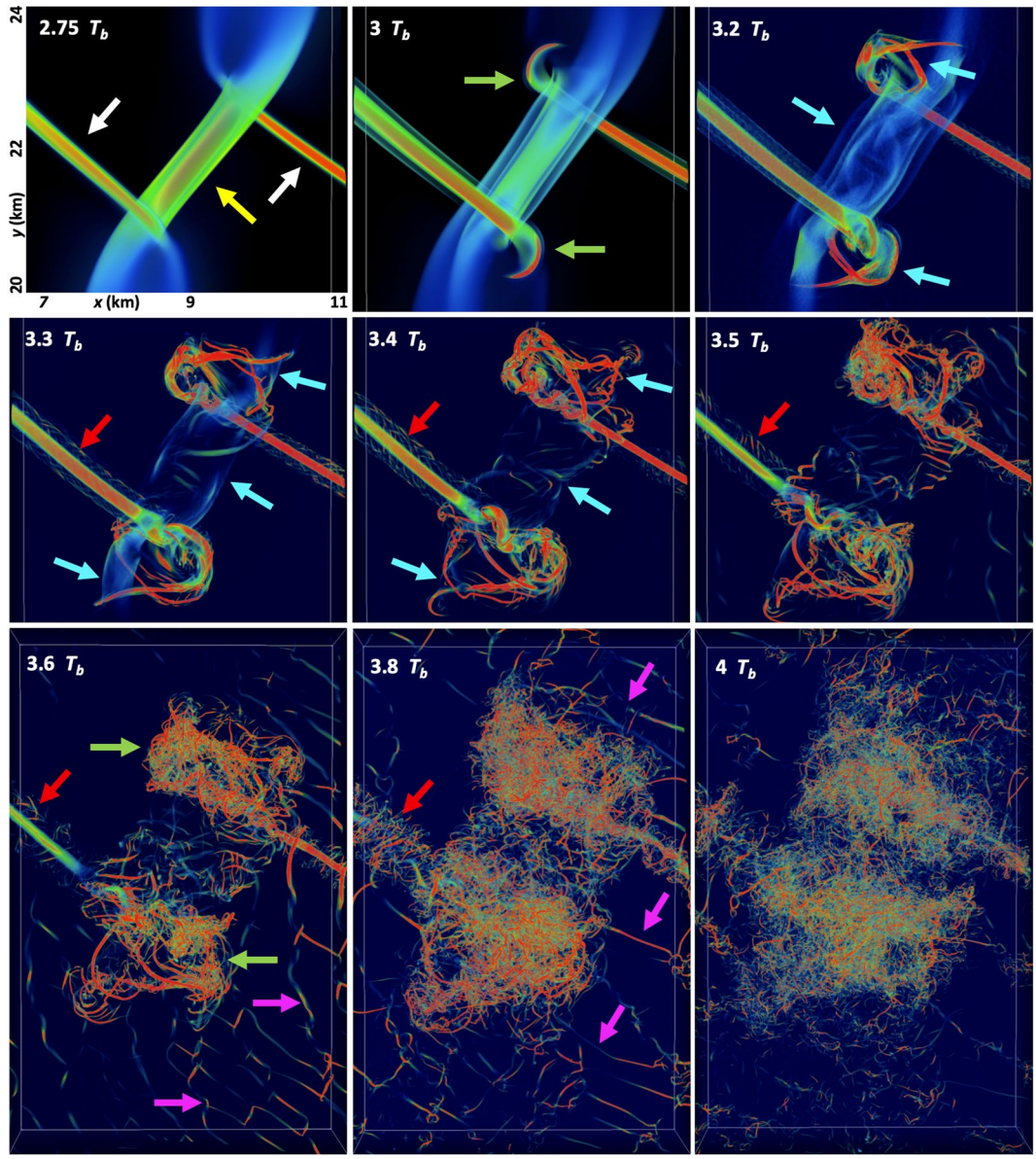

Figure 6. As for Region 1 for Region 2 showing the evolution of two vortex tubes linking to one billow core. Features are labeled using the same arrow colors as in Figure 5. Note the more rapid evolution in this region due to two vortex tubes deforming one billow core.

Given the delayed SIs in the absence of T&K dynamics, 3-D imaging of λ_2 viewed from above is shown for the KH billow at $x \sim$ 13.5–16.5 km and $y =$ 35–40 km from 3.5 to 3.9 T_b in Figure 7. As above, the λ_2 color and opacity scales vary among the 3 times in order to reveal the features of interest at each. The first field at 3.5 T_b shows a confined and relatively uniform billow core and evidence of weak initial secondary CI in the outer billow and KHI both above and below the billow core and on the stratified braid at smaller and larger x (yellow, pink, and white arrows, respectively). We note, for comparison, that these initial SI responses and interactions occur coincident with the initial emergence of turbulence due to T&K dynamics in Regions 1 and 2 shown in Figures 5 and 6.

The small-scale dynamics intensify rapidly and are seen to attain much larger amplitudes and initiate significant interactions by 3.7 T_b and exhibit strong, local nonlinear responses by 3.9 T_b. Secondary CI (pink and red arrows) are much more pronounced at 3.7 T_b, both in the upper billow and in the ascending and descending edges at smaller and larger x, respectively. Secondary KHI (white arrows) also become prominent by 3.7 T_b and interact strongly with, and intensify, the CIs in close proximity by 3.7 T_b.

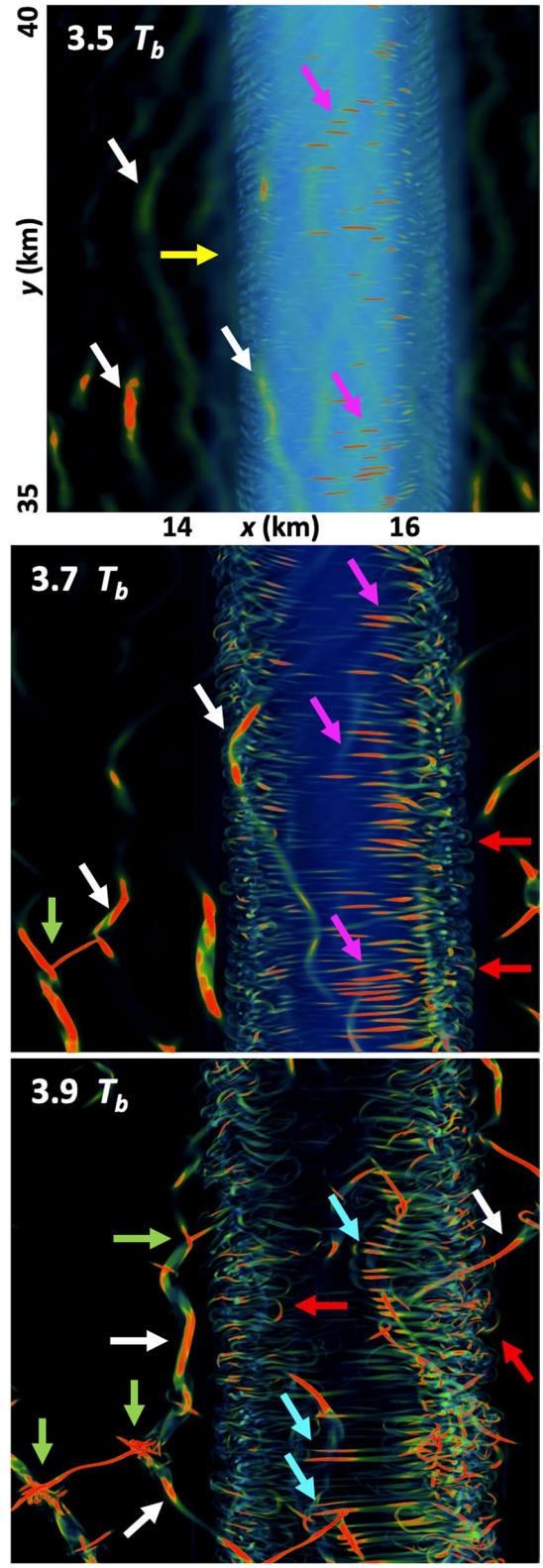

Figure 7. λ_2 (x, y) viewed from above at y = 35–40 km at 3.5, 3.7, and 3.9 T_b. Color and opacity scales vary in time, as above. The arrows show the initial Kelvin-Helmholtz billow core (yellow), secondary KHI (white) and CIs (pink and red), regions where CIs are enhanced in close proximity to secondary KHI (blue), and knots where secondary KHI and vortex tubes link on stratified vortex sheets (green).

The CIs also exhibit formation of vortex loops where they attain finite amplitudes and are especially prevalent at the descending edge of the KH billow at 3.7 and 3.9 T_b (red arrows). These differing responses are due, in part at least, to the apparently stronger secondary KHI at larger y that induce local increases in secondary CI amplitudes where they are in close proximity. See the stronger CIs at lower right appearing to underlie the secondary KHI at 3.7 T_b, and which exhibit much stronger correlations somewhat later (see the blue arrows at 3.9 T_b).

The secondary KHI on the vortex sheet behind the KH billow seen emerging at 3.5 T_b also intensify rapidly thereafter. These exhibit variable orientations despite the dominant $\zeta_y > 0$ of the vortex sheet at this location because of the random initial and secondary noise seeds noted above. Thus, secondary KHI have either $\zeta_x > 0$ or $\zeta_x < 0$, and this results in multiple sites where they resemble the small-scale, secondary KHI T&K dynamics on the vortex sheet discussed in Region 1 and seen at 4 T_b in Figure 5. As in that case, the secondary KHI $\lambda_h \sim 0.1$ of the primary KHI implies a local Re $\sim$ 50 and that these secondary T&K dynamics likely remain laminar.

5. Simulated PMC Imaging and Comparisons With PMC Observations

Synthetic PMC imaging for the KHI fields shown in Figures 3 and 4 viewed from above and in x-z cross sections at y = 13, 22, and 36 km are displayed from 3 to 5 T_b at top and bottom in Figure 8. Subsets of these fields from y = 0–30 km at 4 and 4.5 T_b, and $\beta(x, z)$ at y = 13 and 22 km from 3 to 5 T_b are shown in Figure 9. As noted above, The PMC layer was assumed to be centered at $z = -300$ m and to have a FWHM brightness of 400 m with a 5% saturation (i.e., above peak β) that was intentionally small in order to display the wide range of KHI SI instability dynamics more clearly.

5.1. Influences of Random Initial Conditions on KH Phase and λ_h Variability

PMC fields in Figure 8 at 3 T_b reveal bright, broader (rising) entrainment regions at their left edges, weaker descending edges, and internal bands during initial billow roll-up. Narrower bright bands arise along the edges of emerging vortex tubes roughly orthogonal to, and spanning, adjacent billows at ~13 and 22 km, as discussed above. These features intensify and thin as the billows become deeper by 3.5 T_b, and bright (dark) regions emerge where vortex tubes overlie (underlie) billow cores and initiate knots, but the details of these dynamics occur at scales much smaller than brightness gradients, hence yield no signatures at early times. Secondary CIs and KHI, and smaller vortex tubes, arise in the billow cores and stratified braids between billows at ~3.5 T_b, respectively (see Figures 5–7), and become more prominent, but remain coherent at 4 T_b.

All of these SI dynamics evolve rapidly from 4 to 5 T_b due to continuing strong interactions among closely spaced, roughly orthogonal vortices having different origins. The most prominent are the large-scale vortex tubes and billow cores leading to bright and dark knots that intensify, expand, and break down to smaller features with high β contrast at later stages. Smaller-scale secondary CIs and KHI in the outer billows and entrainment regions are both prominent by 4 T_b, exhibit rapid interactions, and contribute to breakdown within, and separate from, regions of T&K dynamics. Not seen clearly in Figure 8, but noted in the discussions of Figures 5–7, are secondary KHI comprising roughly orthogonal vortex tube segments that form on the vortex sheets between billows, intensify in time, and interact via small-scale T&K dynamics. These various vortex dynamics drive KH billow breakdown, loss of coherence along y, and a cascade to smaller scales that are illustrated in Figure 9 and discussed in greater detail below.

5.2. T&K Dynamics Influences on PMC Imaging and Profiling

Expanded views of PMC β (x, y) from y = 0–30 km at z = 0 are shown at 4 and 4.5 T_b in Figure 9 to illustrate the dynamics accounting for the various PMC responses in β more clearly. β (x, z) at y = 13 and 22 km (bottom, left and right) from 3 to 5 T_b enable identification of key features. Bright and dark bands aligned along the billow axes at 4 T_b arise where billow entrainment from below (above) occurs at their left (right) edges and at interior locations where they are aligned roughly vertically, due to the peak initial β (z) centered below the initial shear layer (see the features noted with orange arrows at top and bottom at 3–4 T_b prior to billow breakdown). Secondary CIs and KHI are seen to emerge at ~3.5 and 4 T_b, respectively, and are shown with black and yellow arrows.

Larger and smaller vortex tubes also arise at earlier and later times, and where the KH billow cores exhibit larger and smaller $d\phi/dy$, respectively (see the red arrows in Figure 9 and the early cross sections in Figures 3 and 4). The larger of these initiate the earlier, large-scale T&K dynamics that precede other SIs discussed in

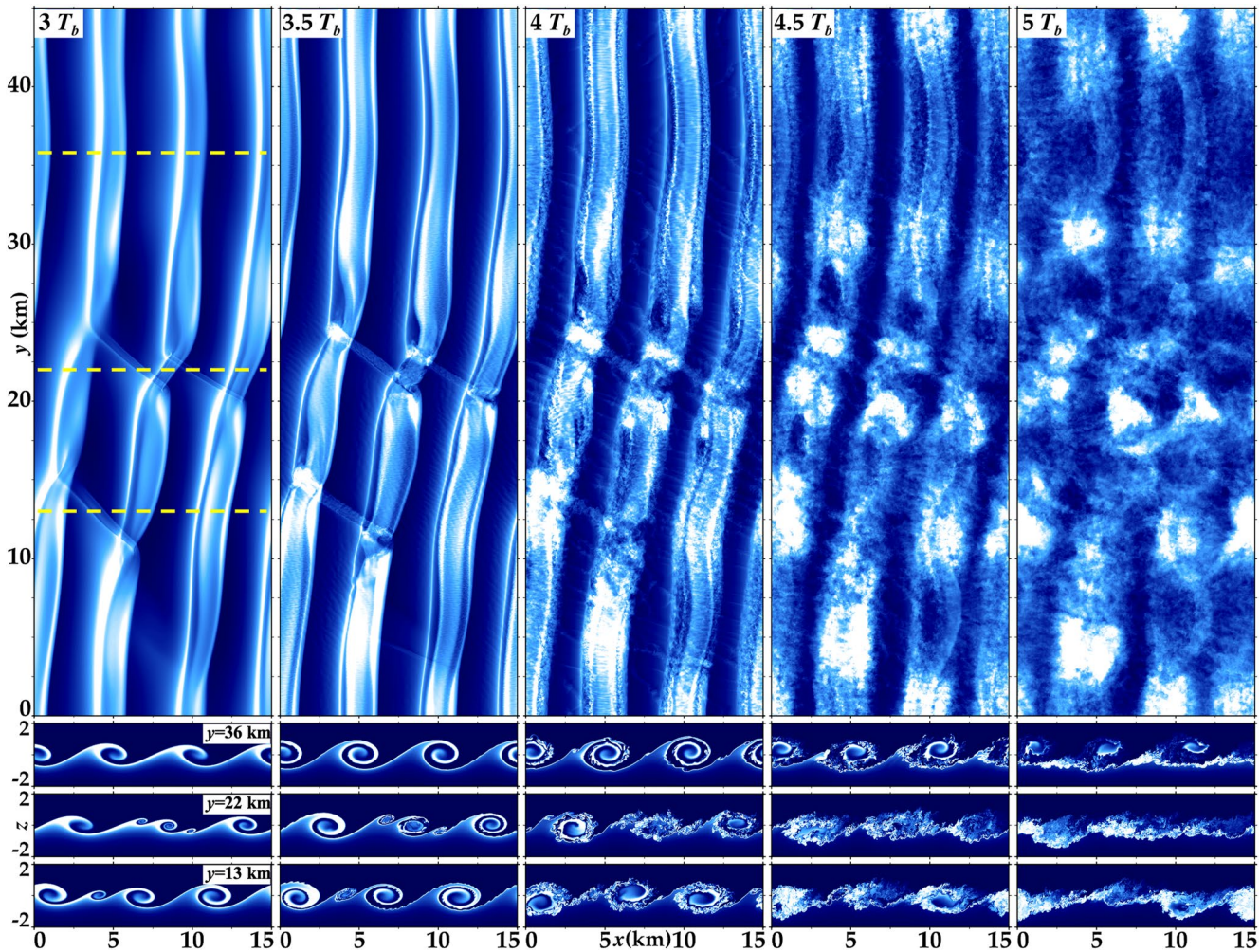

Figure 8. As in Figures 3 and 4 for β (x, y) at $z = 0$ viewed from above (top) and β (x, z) at z = 13, 22, and 36 km viewed from smaller y (bottom) from 3 to 5 T_b. The fields at top are 5% saturated.

Subsections 4.2.1 and 4.2.2 and shown in Figures 5 and 6. These T&K dynamics account for large β where the vortex tubes overlie the KH billows (see green arrows in Figure 9), and smaller β at their other ends at larger x.

Following the initial T&K dynamics in Regions 1 and 2 driving early and strong turbulence transitions, these dynamics break down the initial billow coherence along x seen occurring at later times at bottom in Figure 8. The subsequent interactions noted above (a) between secondary CI and KHI instabilities where they come into close proximity at the KH billow edges and (b) among secondary KHI on the intensifying vortex sheets between adjacent billows were highlighted by red, blue, and green arrows in Figure 7. Evidence of these interactions are highlighted with blue and yellow arrows at 4 T_b in Figure 9. Additional, less distinct vortex tubes continue to arise between distorted billows at late times (see red arrows at right in Figure 9). Finally, all of these vortex interactions drive small-scale 3-D structures at these times (see pink arrows in Figure 9).

5.3. Comparisons of KHI Modeling and PMC Turbo Observations

Our modeling of T&K dynamics described above was necessarily idealized and not guided by specific observations, apart from what was able to be inferred about the character, details, and evolutions of the observed responses at the PMC layer. These include the KH λ_h, billow depths, the presence of GWs apparently modulating the formation and development of the KHI, evidence for the mis-aligned KH billows, and the presence of a wide range of apparent instability types, scales, interactions, and responses. They were also able to be resolved at high

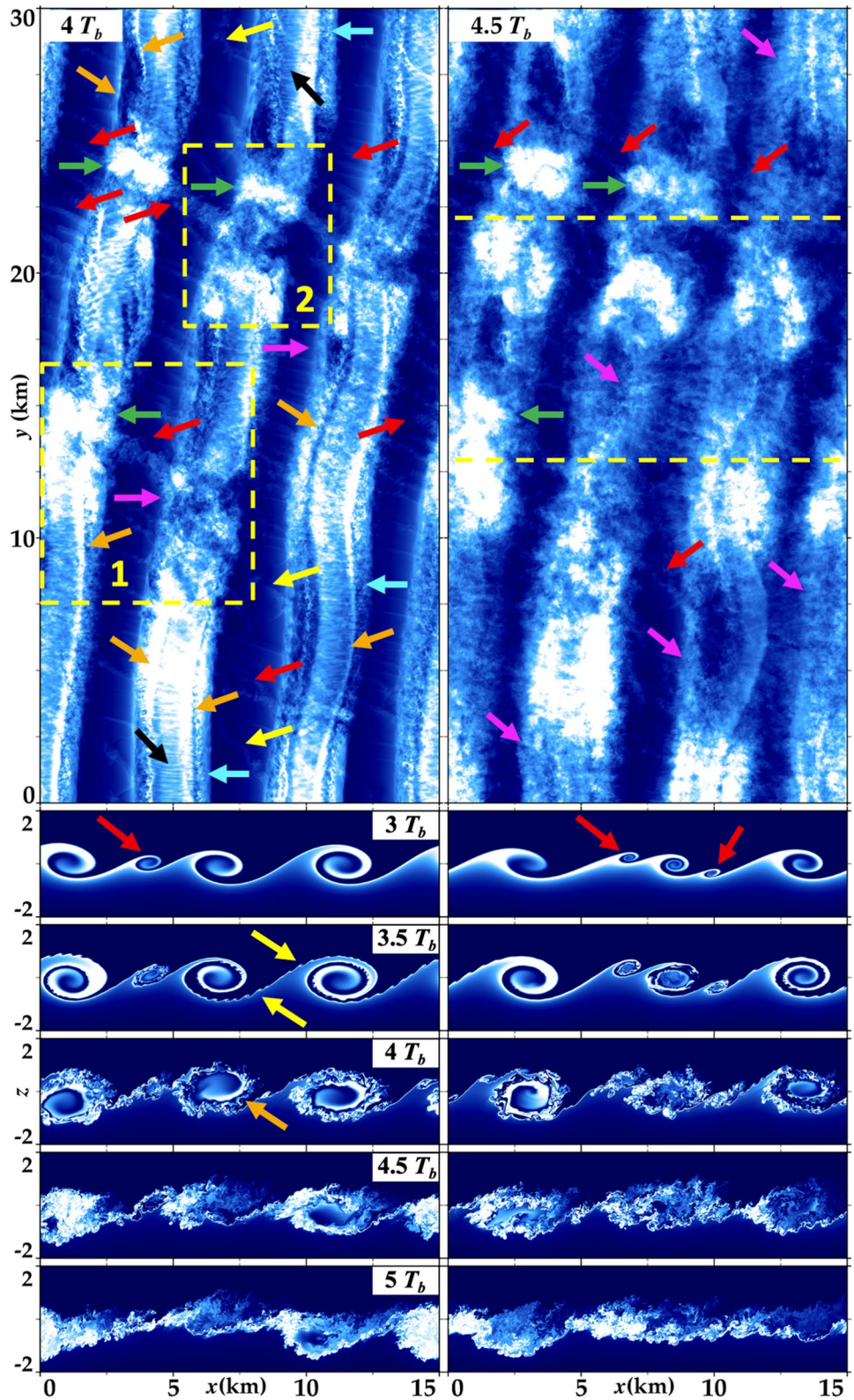

Figure 9. (top) As in Figure 8 at top for y = 0–30 km at 4 and 4.5 T_b. (bottom) As in Figure 8 at bottom at y = 13 and 22 km (left and right from 3 to 5 T_b, top to bottom). Rectangles show the regions addressed in Figures 5 and 6. Arrows indicate large-scale KHI and SIs using the same color codes as in Figure 2.

horizontal and vertical resolution due to a relatively thin PMC layer and sub-layers, enabling confident identification of their scales, character, and evolutions.

The PMC observations demonstrate the presence of KH billows exhibiting apparent T&K dynamics. However, they are not able to provide specific guidance on initial conditions for modeling. This is because T&K responses at finite amplitudes are dictated by weak, very small-scale perturbations to the initial PMC field that are impossible to infer from the PMC imaging, and related features of the initial shear layer that were not observed. Additionally, quantitative modeling requires a triply periodic domain in order to employ a spectral representation of the dynamics to accurately describe their evolutions, interactions among different components, and implications for instabilities, turbulence, and energy dissipation rates. Validation of the model predictions and implications thus relies on identification of "telltale" features of the evolutions of, and key responses to, T&K dynamics seen in the PMC layer in the right sequence.

Comparing the progression of features of initial, large-scale KH billows throughout their evolutions seen in Figures 2, 8, and 9 reveals many common elements. Both the PMC imaging and the modeled PMCs exhibit regions where billows are kinked and/or mis-aligned along their axes and induce large-scale vortex tubes (see the red arrows in Figures 2 and 8). Where initial billows are not perturbed, they exhibit entrainment of air with high (low) β and brighter (darker) bands over (under) the billows and where these layers are oriented approximately vertically at the billows edges (see the orange arrows in these figures). Similar undulating bright/dark boundaries on the vortex sheets between adjacent billows are secondary KHI (yellow arrows in Figures 2 and 9), whereas small-scale, streamwise-aligned, structures seen in the billow edges and interiors are evidence of secondary CIs (black arrows in Figures 2 and 9), based on the analysis of these features in Figures 5–7. The evolutions of regions containing T&K dynamics exhibit the reduction or elimination of β variations perpendicular to the billow axes in both cases (see the black ovals in Figure 2 and the mixing along x in Figures 8 and 9 extending to later times). Finally, both the PMC imaging in Figure 2 and the $\beta(x, y)$ fields in Figure 9 exhibit patchy, small-scale, 3-D structures arising due to breakdown of the larger- and smaller-scale instabilities, both in regions of previous T&K dynamics, and accompanying individual KH billows (see pink arrows in Figures 2 and 9). Importantly, KH billow breakdown is significantly faster accompanying T&K dynamics.

6. Energy Dissipation Rates

Discussions of Figures 4–6, 8, and 9 revealed elevated vorticity dynamics and accelerated energy and enstrophy cascades to smaller scales in regions of strong T&K dynamics relative to less disturbed regions in the computational domain. These imply enhanced turbulence energy dissipation rates, ε, at smaller scales, and elevated local mean ε, denoted $<\varepsilon>$, in these regions. All ε fields and figures discussed below assume a weak background turbulent viscosity of $\nu_{turb} \sim 2.2$ m^2/s, rather than the true $\nu \sim 0.7$ m^2/s at the PMC layer (Dalin et al., 2012), due to the observations reported by K22 showing a very dynamically active GW and instability field.

We illustrate the implications of these vorticity dynamics in different regions with cross sections of $\varepsilon(x, y)$ at $z = 0$ and $\varepsilon(x, z)$ at $y = 13$, 22, and 36 km from 3 to 4.5 T_b in the upper and lower panels of Figure 10 using a $\log_{10}$ color scale spanning two decades. The fields in Figure 10 closely resemble those for $|\zeta|$ in Figure 4 because $<\zeta_i^2(k)>$ and $<\varepsilon(k)/\nu>$ averaged over all y and z must be identical for exact solutions in a periodic domain. They differ locally (but only weakly) due to local fluxes that need not sum to zero over non-periodic sub-domains. The $\varepsilon(x, y)$ cross sections confirm emergence of initial, small-scale turbulence within the knot regions by 3.5 T_b (see Regions 1 and 2 in Figure 4), its rapid intensification throughout the impacted KH billow cores (see the regions highlighted by the dashed lines at $y = 13$ and 22 km), and the enhanced and accelerated turbulence transitions by secondary CI and KHI at these billow edges by 4 T_b. The fields at 4.5 T_b reveal these sites to host the strongest turbulence extending to later times.

$\varepsilon(x, z)$ fields at bottom in Figure 10 confirm the localization of initial T&K turbulence transitions to the vortex tubes and adjacent billow cores (as revealed in the discussions of Figures 5 and 6). They also confirm the accelerated expansion of strong, small-scale turbulence throughout the adjacent billow cores relative to those not impacted by the T&K dynamics. Specifically, billow cores participating in T&K dynamics have broken down fully via twist-wave generation by 3.5 T_b (see Figures 5 and 6) and become fully turbulent by 4 T_b (see Figure 10, upper and lower panels). In contrast, KH billows at these y, but other x, and at y without strong T&K dynamics, reveal emerging secondary CI and KHI at 3.5 T_b, and initial turbulence transitions by 4 T_b. The $\varepsilon(x, z)$ fields also

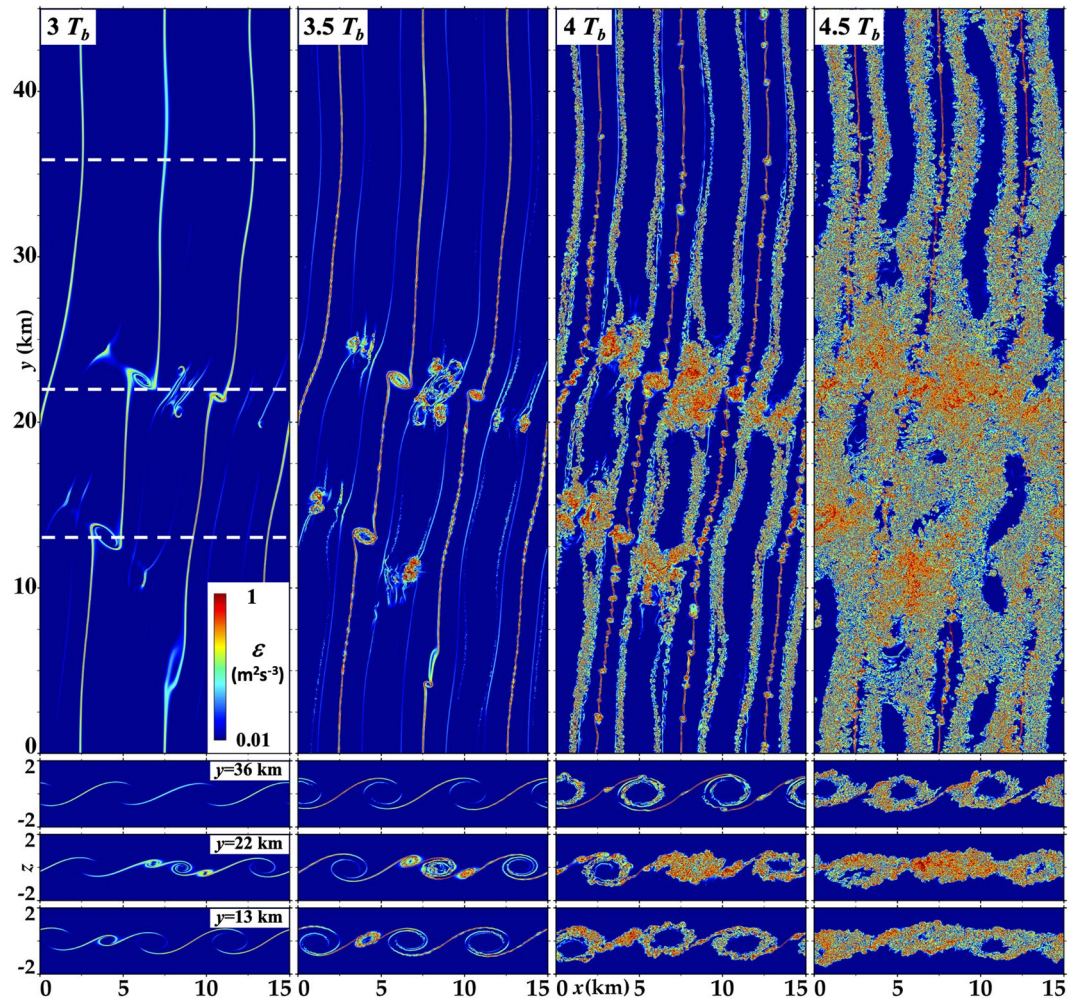

Figure 10. (top) $\varepsilon(x, y)$ at $z = 0$ and (bottom) $\varepsilon(x, z)$ at $y = 13$, 22, and 36 km from 3 to 4.5 T_b on a log scale.

reveal KH billow breakdown at the T&K sites that account for their expansion along x seen at $z = 0$ at top in Figure 10.

We now examine the degree to which T&K dynamics enhance local $<\varepsilon>$ relative to regions not exhibiting these dynamics. For these purposes, we assess $<\varepsilon>(x, y)$ and $<\varepsilon>(y, z)$ via spectral truncation yielding spatial averaging of ~1.5 km in all directions. Resulting $<\varepsilon>(x, y)$ and $<\varepsilon>(y, z)$ at 4, 5, 6, 8, and 10 T_b are shown at top and bottom in Figure 11. Averaging regions are shown with rectangles in the panels at 4 T_b. Probability Density Functions (PDFs) of ε and temporal evolutions of $<\varepsilon>$ in these sub-domains are shown in Figures 12 and 13.

The fields at top in Figure 11 reveal the largest local $<\varepsilon>(x, y)$ to emerge at early times accompanying the T&K dynamics centered at y~13 and 22 km. In each case, the most intense $<\varepsilon>$ occur by 4–4.5 T_b in the evolving, intense knot regions discussed in Subsections 4.2.1 and 4.2.2. $<\varepsilon>(x, y)$ in these regions decrease slowly thereafter (over ~2–3 T_b) because the initial T&K dynamics also yield large-scale twist waves (see Figure 6 from 3 to 4 T_b) that accelerate additional, though weaker, turbulence transitions in adjacent regions along the KH billow cores. Where KH billow alignments exhibit weaker phase variations along y outside regions of T&K dynamics, secondary CIs and KHIs yield enhanced $<\varepsilon>(x, y)$ extending to ~6–7 T_b (see Figure 5 at 3.6–4 T_b).

The $<\varepsilon>(x, z)$ fields at bottom in Figure 11 show the largest $<\varepsilon>$ to be confined within $|z| < 1$ km because billow depths only slightly exceed 2 km and the peak $<\varepsilon>(y, z)$ occur at smaller $|z|$ (see the lower panels of Figures 3, 4, and 8). Also seen in both fields is evidence that $<\varepsilon>(y, z)$ in Region a exhibits a second, larger peak after 6 T_b and that in Region b remains large to beyond 6 T_b. In contrast, $<\varepsilon>(y, z)$ in Region c remains much smaller than in Regions a and b, but nevertheless exhibits a weak, initial peak at ~5 T_b and an extended weaker, secondary

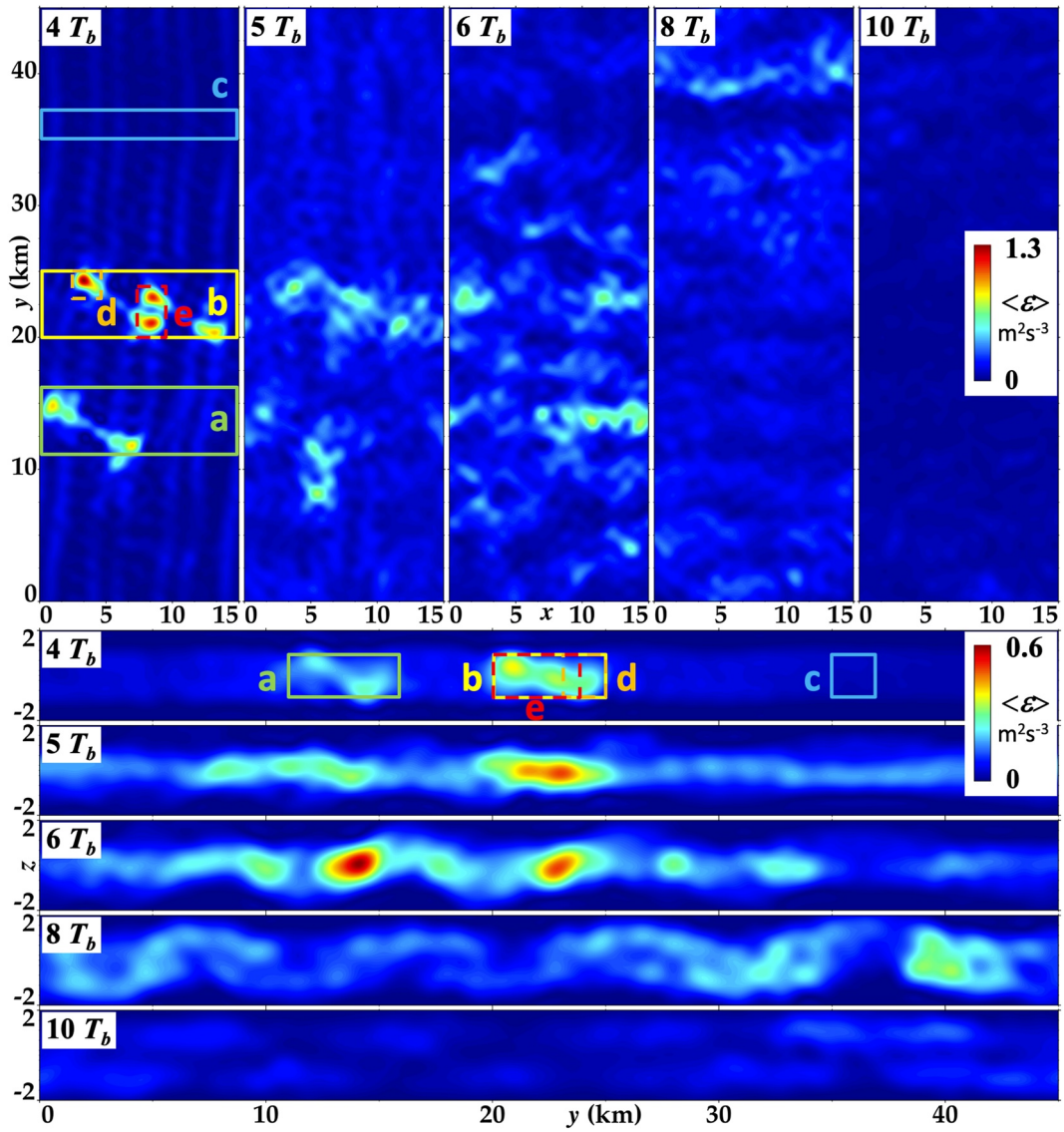

Figure 11. (top) $<\varepsilon>(x, y)$ and (bottom) $<\varepsilon>(y, z)$ at 4–10 T_b averaged over $|z| < 1$ km and all x, respectively. Solid and dashed rectangles show regions of more limited averaging denoted a-e. A linear $<\varepsilon>$ color scale is used for all panels in this case to reveal relative intensities more clearly.

peak thereafter. The sources of the latter of these can be traced to shear layer vertical displacements along y seen emerging in the $<\varepsilon>(y, z)$ fields (Figure 11, bottom) beginning ~5 T_b and having large amplitudes to at least 8 T_b. These displacements induce differential stretching and intensification of the vortex sheets wrapping around and between adjacent KH billows that enhance secondary CI, KHI, and larger-scale vortex tubes, which in turn drive secondary T&K dynamics, stronger turbulence transitions, and larger local $<\varepsilon>$ than would occur in their absence.

6.1. Energy Dissipation Rate PDFs and Evolutions

To quantify ε distributions and $<\varepsilon>$ induced by local, and non-local, T&K dynamics, $\log_{10}\varepsilon$ PDFs in Regions a, b, and c in Figure 11 centered at $y = 13$, 22, and 36 km, and in Regions d and e centered on several initial knots, are shown at left and right, respectively, in Figure 12 from 4 to 8 T_b. All PDFs at 4 T_b include significant contributions from non-turbulent regions because initial turbulence is localized at this time, though more widespread in regions of T&K dynamics than elsewhere (see Figures 5–7 and 10 at 4 T_b). Turbulence intensifies and expands rapidly in all these regions by ~5–6 T_b, but remains much less intense in Region c having only weak T&K influences.

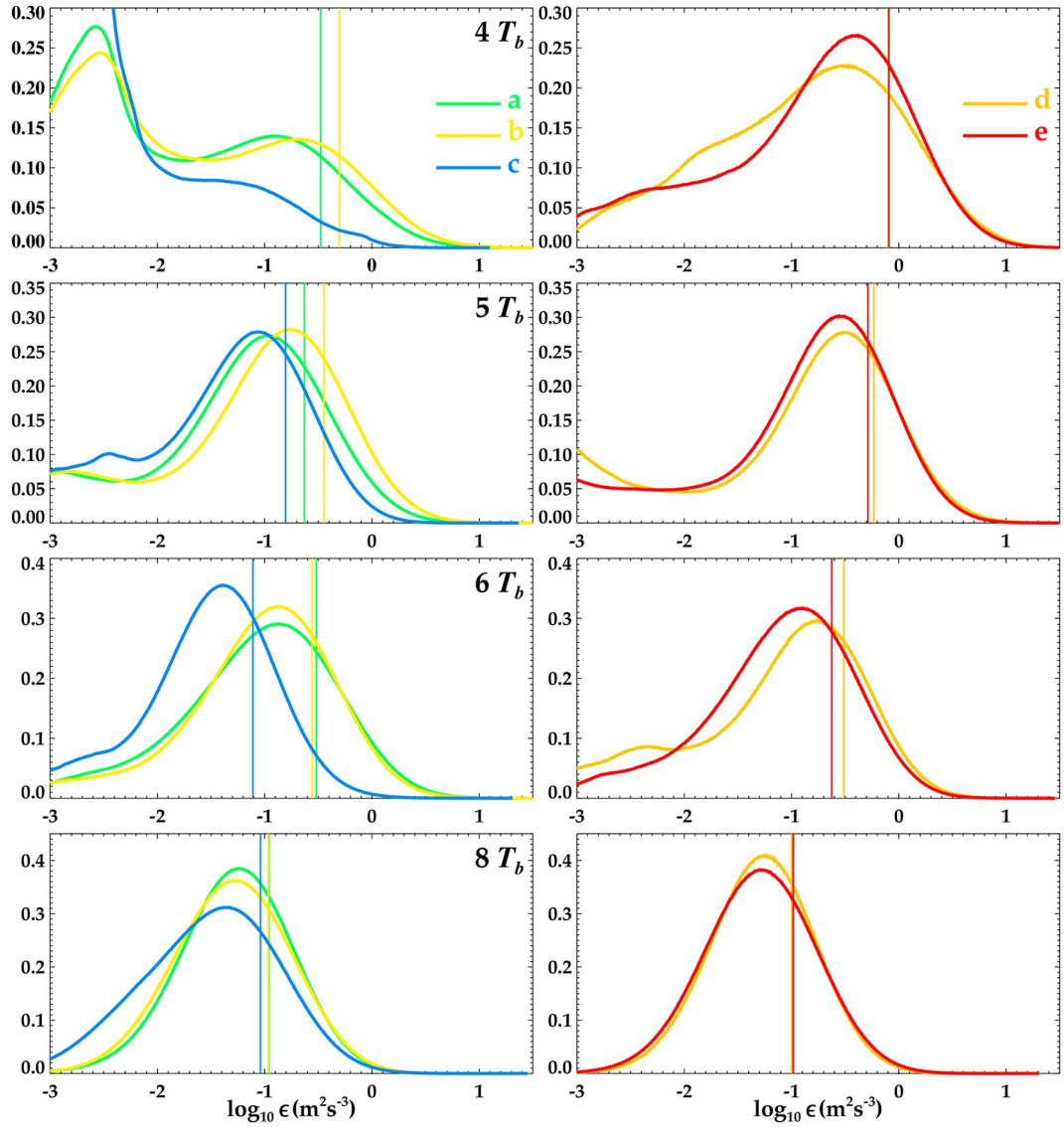

Figure 12. Probability Density Functions (PDFs) of $\log_{10}\varepsilon$ in Regions a, b, and c (d and e) in the left (right) columns at 4, 5, 6, and 8 T_b (top to bottom). Vertical lines indicate $\log_{10}<\varepsilon>$ for each PDF inferred as described in the text. Line colors are as in Figure 11.

Interestingly, the PDFs for these diverse regions exhibit similar shapes and widths throughout their evolutions despite their different sources and varying evolutions.

Estimated $\log_{10}<\varepsilon>$ are obtained assuming symmetric, approximately log-normal PDFs centered on the respective PDF peaks where these are clearly defined. This assumes zero skewness in the PDFs, as appears justified in the T&K regions at later times. However, the PDFs reveal increasing kurtosis becoming as large as ~10–12 at 8 T_b (and thereafter) in all regions.

Figures 10–12 reveal that a significant fraction of the shear layer exhibits no turbulence at 4 T_b, despite initial turbulence transitions beginning by ~3.2 T_b in the T&K regions and prior to 4 T_b without these dynamics. To intercompare the turbulence evolutions in the various regions identified above more quantitatively, time series of the evolving $<\varepsilon>$ in Regions a, b, c, d, and e, from 3.8 to 9 T_b are shown with dashed lines in Figure 13. Additionally, $<\varepsilon>$ estimated for only the turbulent portions of these regions as described above are shown with solid lines.

The $<\varepsilon>$ estimates including and excluding non-turbulent portions differ by up to a factor of ~2 at ~4–4.5 T_b at most sites and approaching 6 T_b in Region d. Of these, Regions d and e containing one and two initial knots,

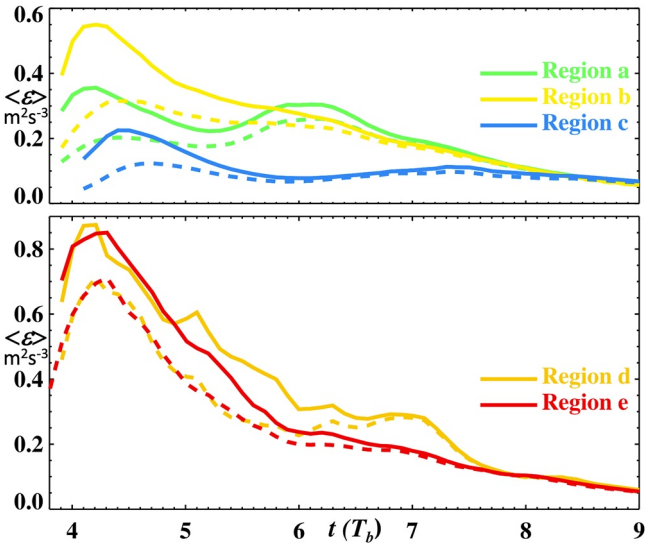

Figure 13. Temporal evolutions of <ε> in Regions a–c (top) and Regions d and e (bottom) for the full regions (dashed) and the portions estimated to be turbulent from symmetric fits centered on the PDF peaks (solid) from 3.8 to 9 T_b (see text for details). Line codes are shown at upper right in each panel; units are m^2s^{-3}.

respectively, accompanying the two vortex tubes interacting with a common billow core yield the largest <ε>. These maxima are more than twice that for Region b containing Regions d and e at early times, but converge by ~7 T_b as turbulence spreads throughout the shear layer. Region a containing a single vortex tube linking two adjacent KH billow cores yields <ε> that are smaller initially, but also attain comparable values to Regions b, d, and e by ~6 T_b. By comparison, Region c having weak or no T&K influences exhibits weaker turbulence by ~2–5 times averaged over the evolutions displayed. Despite their very different initial vortex dynamics, <ε> in all regions converge to within a few % by 8 T_b and thereafter.

6.2. Velocity Variance and Energy Dissipation Rate Spectra

As seen in Equation 6, the spatial resolution required to attain true DNS, $\Delta x < 1.8\ (\nu^3/\varepsilon)^{1/4}$, is dictated by the need to resolve the large majority of the ε spectrum. This requires resolution increases by ~5–10 times relative to that needed to resolve the evolving KHI and initial SIs as turbulence emerges and intensifies. In this application, a maximum of 3,240 spectral modes were required due to the large Re specified to enable secondary KHI and examination of the relative contributions of the various SIs. This yielded spatial resolution spanning 3 decades extending to 0.003 KHI λ_x with the $2/3^{rds}$ truncation required to remove spectral aliasing.

Spectra of <u_i^2>, <$\varepsilon(k)$>, and dissipation content, k<$\varepsilon(k)$>, along x are shown (left to right) for Regions a-c (top to bottom) in Figure 14. The <u_i^2> spectra at left all exhibit distinct peaks at $k = 2\pi$ n/3 $\lambda_x = k_n$, for $n = 3, 6, 9, \ldots$ at 3 T_b (for a primary KHI $\lambda_x = 2\pi/k_3$) and extending up to 2 T_b thereafter where T&K dynamics are weaker or absent. These are signatures of initial KH billows largely in u' and w'. The peaks are also seen, but more weakly after 3 T_b, in the <$\varepsilon(k)$> and k<$\varepsilon(k)$> spectra at center and right due to billow breakdown beginning ~4–4.5 T_b (see Figure 10, bottom).

Variance spectra in Regions a and b attain peak amplitudes and roughly −5/3 slopes extending from $k \sim k_3$ to k_{100} or larger by 5 T_b in response to strong turbulence generation by the major T&K dynamics arising at those sites. Those in Region c are delayed and weaker (by ~2–3 times) due to the emergence of adjacent, weaker T&K dynamics only from ~6 to 8 T_b. The <$\varepsilon(k)$> spectra in the center column in Regions a and b reveal weak dissipation extending throughout much of the inertial range (to $k \sim 100k_n$), but fall off rapidly into the viscous range. The k<$\varepsilon(k)$> spectra at right provide a more quantitative comparison of the <ε> dissipation rates and scales among the three sites. Their decay by the Nyquist wavenumber confirm that the large majority of kinetic energy dissipation occurs at resolved scales at all sites and times, as required for a DNS of these dynamics.

7. Discussion

KHI have been known for over 50 years to be common throughout the atmosphere, to occur at increasing horizontal wavelengths with increasing altitude, and to drive local mixing and transport via SIs leading to turbulence (see references cited in the Introduction). Initial atmospheric observations were unable to resolve the SIs accounting for these turbulence transitions because ground-based imaging did not have such capabilities at those times. However, SIs of KHI were seen in tilt-tank shear flow studies and described in detail in early and more recent studies by Thorpe (1973a, 1973b, 1985, 1987, 2002), Schowalter et al. (1994), and Caulfield et al. (1996). Of these, Thorpe first noted the occurrence in laboratory studies of a new type of SI arising where KH billows are mis-aligned or discontinuous along their axes, which he termed "knots," given their origins accompanying entwining of initially orthogonal vortices. Thorpe (2002) also noted the frequent occurrence of such features in tropospheric clouds and suggested that they may be due to GWs propagating along KH billow axes and modulating the shear parameters and resulting Ri.

The first clear observation of a KHI T&K event in the atmosphere was performed with high-resolution OH airglow imaging supported by Na lidar profiling of temperatures and winds at the ALO at Cerro Pachon, Chile (Hecht et al., 2021). That study employed difference imaging to reveal small-scale SI features including (a) CIs

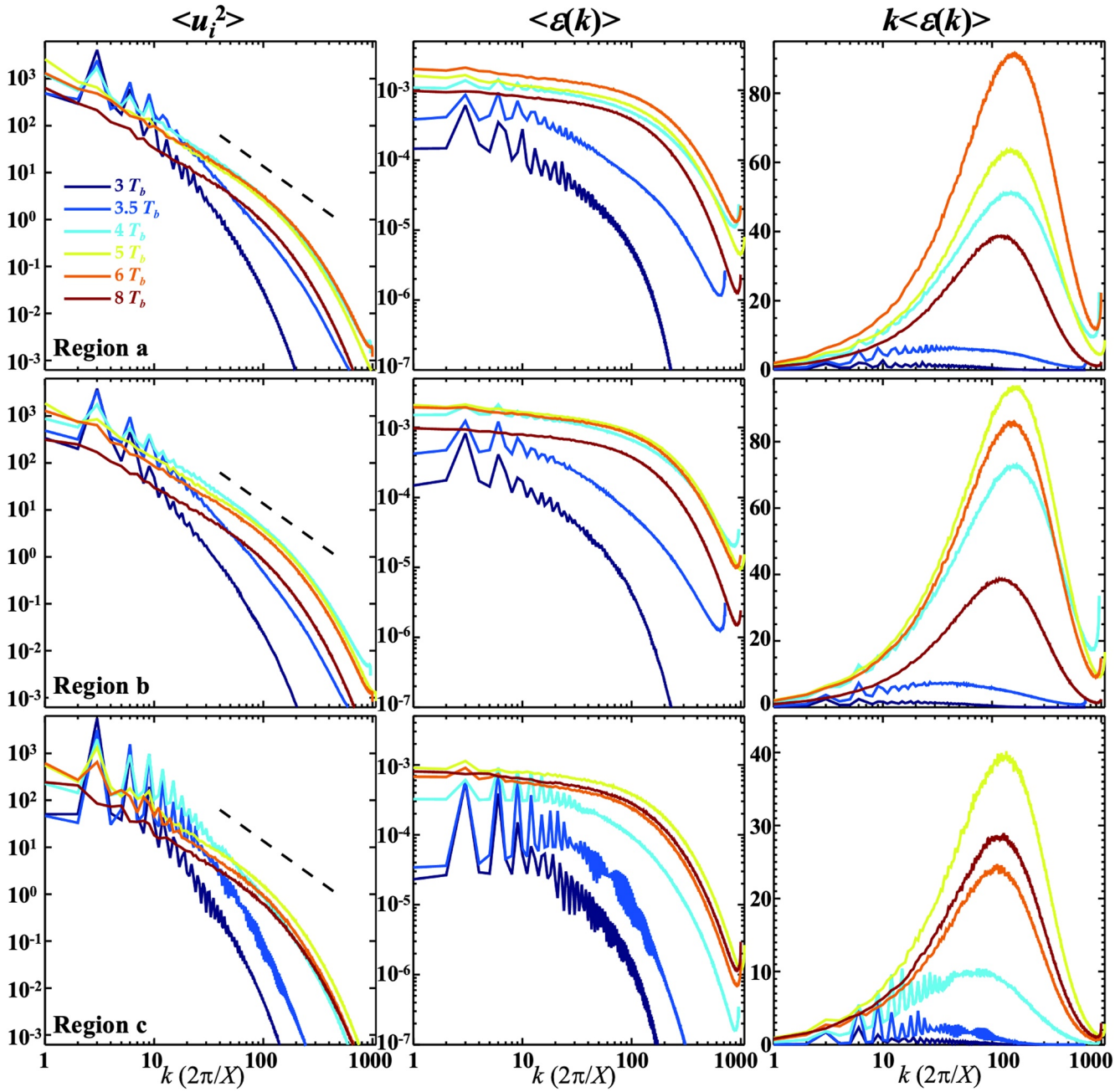

Figure 14. $<u_i^2(k)>$, $<\varepsilon(k)>$, and $k<\varepsilon(k)>$ in Regions a, b, and c centered at y = 13, 22, and 36 km (top to bottom) from 3 to 8 T_b (see color codes at top left). Those in Regions a and b are averaged over $|\Delta y| < 2.5$ km and $|\Delta z| < 1$ km; those in Region c are averaged over only $|\Delta y| < 1$ km and $|\Delta z| < 1$ km. The dashed black lines at left show a −5/3 slope.

within individual KH billow cores, (b) vortex tubes extending between, and linking, adjacent billow cores, and (c) vortex knots that formed where two KH billow "ends" linked to one in regions where the billow cores were mis-aligned along their axes. Hecht et al. (2021) employed an energetics argument to infer an $\varepsilon \sim 1$ m^{2}s^{-3} for one portion of this event.

A companion paper to Hecht et al. (2021) by Fritts et al. (2021) performed an idealized, high-resolution, compressible simulation of KHI T&K dynamics arising from mis-aligned billow cores that described emerging vortex tubes and SIs, their interactions leading to knot formation, and their increasing complexity with time. However, this study was unable to confirm the ε estimated by Hecht et al. (2021) because the compressible model resolution did not enable a description of these vortex dynamics spanning the dissipation range of turbulence.

By comparison, results presented here used a spectral description of multi-scale KHI dynamics seeded with weak white noise. Resolution was increased as turbulence arose and intensified, so as to ensure compliance with the DNS constraint on resolution at all times. These results enabled detailed exploration of the vortex dynamics driving turbulence transitions in, and exterior to, T&K dynamics, and quantitative comparisons of ε statistics and $<\varepsilon>$ among sites. Distributions of ε were found to be nearly log-normal, but to exhibit large kurtosis at later stages indicating elevated occurrences of intense turbulence as $<\varepsilon>$ decreased. $<\varepsilon>$ in regions of initial T&K dynamics achieved maximum values of ∼0.3–0.9 m^2s^{-3} for the KHI $\lambda_h \sim 5$ km and estimated Ri = 0.1 described by K22, and these are ∼2–4 times larger than seen to arise in regions without T&K influences.

These results can be scaled to other events having different KHI λ_h, as $<\varepsilon> \sim \lambda_h^2$ for those having similar Re and Ri. The KHI event analyzed by Chau et al. (2020) revealed horizontal structures suggestive of T&K dynamics (see their Figure 5), but at an inferred Ri likely larger than used in our DNS. Their inferred $<\varepsilon> \sim 1$ m^2s^{-3} is nevertheless consistent with the scaled DNS values for their KHI λ_h∼8 km. The comparable estimate for $<\varepsilon>$ by Hecht et al. (2021) for KHI exhibiting clear T&K dynamics for unknown Ri is likewise consistent with our DNS results scaled to a KHI λ_h∼8 km. Both these comparisons are qualitative, however, due to their unknown Ri. The Mesquita et al. (2020) estimate of $<\varepsilon> \sim 38$ m^2s^{-3} at 102 km for KH billows having $\lambda_h \sim 9.8$ km is ∼10–30 times larger than our largest DNS estimate scaled to the same KH billow λ_h at the times of most intense T&K dynamics. Such very large $<\varepsilon>$ would seem to require a significantly smaller Ri than modeled here. This not impossible in the strongly sheared and variable environments in the lower thermosphere, but such simulations have not been performed, and more quantitative measurements would be beneficial, given the apparent need for more mixing at these altitudes (see below).

8. Summary and Conclusions

DNS modeling of idealized multi-scale KHI dynamics described here was motivated by recent, high-resolution imaging of such an event identified during the PMC Turbo experiment and described by K22. A random noise seed led to varying initial KHI wavelengths and phases that imposed significant phase gradients, $d\phi/dy > 0$, along their axes in finite-amplitude KH billows thereafter. Regions of significant $d\phi/dy > 0$ induced T&K dynamics that compared qualitatively with the analysis by K22, including secondary CIs and KHIs, vortex tubes, and T&K dynamics resulting from vortex tube and KH billow core interactions.

Regions of T&K dynamics were found to exhibit more rapid turbulence transitions and stronger turbulence intensities than regions exhibiting only secondary CIs and KHIs of individual KH billows, with enhancements of $<\varepsilon>$ as large as ∼2–5 times initially and that remained elevated for multiple T_b. Importantly, these enhanced $<\varepsilon>$ accompanied mis-aligned, or kinked, KH billow cores rather than discontinuous billow cores, such as were seen by K22 and by Hecht et al. (2021) in a similar event observed over ALO. Compressible modeling accompanying the ALO event by Fritts et al. (2021) specifically targeted T&K dynamics of discontinuous billow cores and revealed other large-scale, intense vortex dynamics. However, that study did not employ a DNS, so was unable to assess turbulence intensities. The potential for these additional T&K dynamics to contribute other sources of enhanced turbulence is suggested by the results of this modeling study. However, their influences remains to be assessed for realistic ranges of Re, Ri, and varying environments and initial conditions.

T&K dynamics of mis-aligned and/or discontinuous KH billow cores may play important, but not yet fully explored or understood roles in the atmosphere, the oceans, and in other stratified and sheared geophysical fluids at sufficiently high Re. As examples, several authors have noted a deficiency in the required mixing based on observed and modeled constituent profiles in the lower thermosphere (Garcia et al., 2014; Liu, 2021; and references therein), to which enhanced mixing due to widespread KHI T&K dynamics appears likely to contribute. In this regard, we note that multiple previous analyses of KHI dynamics seen in airglow and PMC imaging reveal larger-scale distortions, mis-alignments, and/or discontinuous KHI billows to be more the rule than the exception (Baumgarten & Fritts, 2014; Fritts et al., 2014; Hecht et al., 2005, 2021). There is also significant evidence for large-scale KHI due to sustained strong shears in the lower thermosphere (Hysell et al., 2012, 2018; Larsen, 2002; Mesquita et al., 2020). The same is expected in the lower atmosphere, where Thorpe (2002) drew attention to evidence for such KH billow mis-alignments in thin tropospheric clouds. KHI T&K dynamics may also contribute significantly to enhanced mixing in the oceans, where small-scale mixing drives abyssal water upwelling (Ferrari et al., 2016).

The emerging evidence for widespread KHI T&K dynamics noted above, and for their enhanced instability dynamics and energy dissipation rates revealed in modeling to date, provide significant motivations for additional DNS exploration of these dynamics. We anticipate that a major discovery employing new modeling, and quantitative measurements when such become possible, will be that KHI T&K dynamics will yield significant turbulence, mixing, and transport where they were not previously anticipated (e.g., shear flows at lower Re and/or higher Ri) based on KHI modeling not addressing these dynamics. This would have major implications for needed improvements in parameterizations of these KHI T&K dynamics from the SBL to the lower thermosphere, and likely also in the oceans.

Data Availability Statement

A link to high-resolution PMC Turbo imaging is provided at https://doi.org/10.13020/df2m-a470. A description of the DNS model data is provided in the Supplemental Materials document. Researchers interested in access to partial data sets should contact the lead author, as full data volumes are enormous (see the Supplemental Materials file).

Acknowledgments
Research described here was supported by the Air Force Office of Scientific Research (AFOSR, grant FA9550-18-1-0009), NASA (grant 80NSSC17K0050), and NSF (grants AGS-1744801, AGS-1758293, AGS-2032678, and AGS-2128443) cited in GEMS. We also acknowledge the DoD High Performance Computing Modernization Program for access to supercomputer platforms that allowed the SAM simulations reported here.

References

Andreassen, Ø., Hvidsten, P. Ø., Fritts, D. C., & Arendt, S. (1998). Vorticity dynamics in a breaking gravity wave, 1, Initial instability evolution. *Journal Fluid Mechanics*, *367*, 27–46. https://doi.org/10.1017/s0022112098001645

Arendt, S., & Fritts, D. C. (1998). The instability of a vortex tube in a weak external shear and strain. *Physics of Fluids*, *10*(2), 530–532. https://doi.org/10.1063/1.869576

Arendt, S., Fritts, D. C., & Andreassen, Ø. (1997). The initial value problem for Kelvin vortex waves. *Journal of Fluid Mechanics*, *344*, 181–212. https://doi.org/10.1017/s0022112097005958

Balsley, B. B., & Carter, D. A. (1982). The spectrum of atmospheric velocity fluctuations at 8 and 86 km. *Geophysical Research Letters*, *9*(4), 465–468. https://doi.org/10.1029/gl009i004p00465

Baumgarten, G., & Fritts, D. C. (2014). Quantifying Kelvin-Helmholtz instability dynamics observed in Noctilucent clouds: 1. Methods and observations. *Journal of Geophysical Research: Atmospheres*, *119*(15), 9324–9337. https://doi.org/10.1002/2014JD021832

Blumen, W., Banta, R., Burns, S. P., Fritts, D. C., Newsom, R., Poulos, G. S., & Sun, J. (2001). Turbulence statistics of a Kelvin–Helmholtz billow event observed in the nighttime boundary layer during the Cooperative Atmosphere–Surface Exchange Study field program. *Dynamics of Atmospheres and Oceans*, *34*(2–4), 189–204. https://doi.org/10.1016/s0377-0265(01)00067-7

Browand, F. K., & Winant, C. D. (1973). Laboratory observations of shear-layer instability in a stratified field. *Boundary-Layer Meteorology*, *5*(1–2), 67–77. https://doi.org/10.1007/bf02188312

Browning, K. A., & Watkins, C. D. (1970). Observations of clear air turbulence by high power radar. *Nature*, *227*(5255), 260–263. https://doi.org/10.1038/227260a0

Caulfield, C. P., Yoshida, S., & Peltier, W. R. (1996). Secondary instability and three-dimensionalization in a laboratory accelerating shear layer with varying density differences. *Dynamics of Atmospheres and Oceans*, *23*(1–4), 139–153. https://doi.org/10.1016/0377-0265(95)00418-1

Chapman, D., & Browning, K. A. (1997). Radar observations of wind-shear splitting within evolving atmospheric Kelvin-Helmholtz billows. *Quarterly Journal of the Royal Meteorological Society*, *123*(541), 1433–1439. https://doi.org/10.1002/qj.49712354114

Chau, J. L., Urco, J. M., Avsarkisov, V., Vierinen, J. P., Latteck, R., Hall, C. M., & Tsutsumi, M. (2020). Four-dimensional quantification of Kelvin-Helmholtz instabilities in the polar summer mesosphere using volumetric radar imaging. *Geophysical Research Letters*, *47*(1), e2019GL086081. https://doi.org/10.1029/2019GL086081

Coulman, C. E., Vernin, J., & Fuchs, A. (1995). Optical seeing-Mechanism of formation of this turbulent laminae in the atmosphere. *Applied Optics*, *34*(24), 5461–5474. https://doi.org/10.1364/ao.34.005461

Dalin, P., Kirkwood, S., Hervig, M., Mihalikova, M., Mikhaylova, D., Wolf, I., & Osepian, A. (2012). Wave influence on polar mesosphere summer echoes above wasa: Experimental and model studies. *Annales Geophysicae*, *30*(8), 1143–1157. https://doi.org/10.5194/angeo-30-1143-2012

Eaton, F., Mclaughlin, S. A., & Hines, J. R. (1995). A new frequency-modulated continuous wave radar for studying planetary boundary layer morphology. *Radio Science*, *30*(1), 75–88. https://doi.org/10.1029/94RS01937

Ferrari, R., Mashayek, A., McDougall, T. J., Nikurashin, M., & Campin, J. M. (2016). Turning ocean mixing upside down. *Journal of Physical Oceanography*, *46*(7), 2239–2261. https://doi.org/10.1175/JPO-D-15-0244.1

Fritts, D. C. (1984). Shear excitation of atmospheric gravity waves. Part II: Nonlinear radiation from a free shear layer. *Journal of the Atmospheric Sciences*, *41*(4), 524–537. https://doi.org/10.1175/1520-0469(1984)041<0524:seoagw>2.0.co;2

Fritts, D. C., & Alexander, M. J. (2003). Gravity dynamics and effects in the middle atmosphere. *Reviews of Geophysics*, *41*(1). https://doi.org/10.1029/2001RG000106

Fritts, D. C., Arendt, S., & Andreassen, O. (1998). Vorticity dynamics in a breaking internal gravity wave, 2. Vortex interactions and transition to turbulence. *Journal of Fluid Mechanics*, *367*, 47–65. https://doi.org/10.1017/s0022112098001633

Fritts, D. C., Arendt, S., & Andreassen, O. (1999). The vorticity dynamics of instability and turbulence breaking internal gravity wave. *Earth Planets and Space*, *51*(7–8), 457–473. https://doi.org/10.1186/bf03353208

Fritts, D. C., Baumgarten, G., Wan, K., Werne, J. A., & Lund, T. (2014). Quantifying Kelvin-Helmholtz instability dynamics observed in Noctilucent clouds: 2. Modeling and interpretation of observations. *Journal of Geophysical Research*, *119*(15), 9324–9337. https://doi.org/10.1002/2014jd021833

Fritts, D. C., & Rastogi, P. K. (1985). Convective and dynamical instabilities due to gravity wave motions in the lower and middle atmosphere: Theory and observations. *Radio Science*, *20*(6), 1247–1277. https://doi.org/10.1029/rs020i006p01247

Fritts, D. C., Wan, K., Franke, P., & Lund, T. (2012). Computation of clear-air radar backscatter from numerical simulations of turbulence: 3. Off-Zenith measurements and biases throughout the lifecycle of a Kelvin-Helmholtz instability. *Journal of Geophysical Research*, *117*(D17), D17101. https://doi.org/10.1029/2011JD017179

Fritts, D. C., Wang, L., Geller, M. A., Lawrence, D. A., Werne, J., & Balsley, B. B. (2016). Numerical modeling of multi-scale dynamics at a high Reynolds number: Instabilities, turbulence, and an assessment of Ozmidov and Thorpe scales. *Journal of the Atmospheric Sciences*, *73*(2), 555–578. https://doi.org/10.1175/JAS-D-14-0343.1

Fritts, D. C., Wang, L., Werne, J., Lund, T., & Wan, K. (2009a). Gravity wave instability dynamics at high Reynolds numbers, 1: Wave field evolution at large amplitudes and high frequencies. *Journal of the Atmospheric Sciences*, *66*(5), 1126–1148. https://doi.org/10.1175/2008JAS2726.1

Fritts, D. C., Wang, L., Werne, J., Lund, T., & Wan, K. (2009b). Gravity wave instability dynamics at high Reynolds numbers, 2: Turbulence evolution, structure, and anisotropy. *Journal of the Atmospheric Sciences*, *66*(5), 1149–1171. https://doi.org/10.1175/2008JAS2727.1

Fritts, D. C., Wang, L., & Werne, J. A. (2013). Gravity wave-fine structure interactions. Part I: Influences of fine structure form and orientation on flow evolution and instability. *Journal of the Atmospheric Sciences*, *70*(12), 3710–3734. https://doi.org/10.1175/JAS-D-13-055.1

Fritts, D. C., & Werne, J. A. (2000). Turbulence dynamics and mixing due to gravity waves in the lower and middle atmosphere. *Geophysical Monograph-American Geophysical Union*, *123*, 143–160.

Fritts, D. C., Wieland, S. A., Lund, T. S., Thorpe, S. A., & Hecht, J. H. (2021). Kelvin-Helmholtz billow interactions and instabilities in the mesosphere over the Andes lidar observatory: 2. Modeling and interpretation. *Journal of Geophysical Research: Atmospheres*, *125*(1), e2020JD033412. https://doi.org/10.1029/2020JD033412

Garcia, R. R., Lopez-Puertas, M., Funke, B., Marsh, D. R., Kinnison, D. E., Smith, A. K., & Gonzalez-Galindo, F. (2014). On the distribution of CO_2 and CO in the mesosphere and lower thermosphere. *Journal of Geophysical Research: Atmospheres*, *119*(9), 5700–5718. https://doi.org/10.1002/2013JD021208

Hannawald, P., Schmidt, C., Wüst, S., & Bittner, M. (2016). A fast SWIR imager for observations of transient features in OH airglow. *Atmospheric Measurement Techniques*, *9*(4), 1461–1472. https://doi.org/10.5194/amt-9-1461-2016

Hecht, J. H. (2004). Instability layers and airglow imaging. *Reviews of Geophysics*, *42*(1), RG1001. https://doi.org/10.1029/2003RG000131

Hecht, J. H., Fritts, D. C., Gelinas, L. J., Rudy, R. J., Walterscheid, R. L., & Liu, A. Z. (2021). Kelvin-helmholtz billow interactions and instabilities in the mesosphere over the Andes lidar observatory: 1. Observations. *Journal of Geophysical Research*, *126*, e2020JD033414. https://doi.org/10.1029/2020JD033414

Hecht, J. H., Liu, A. Z., Walterscheid, R. L., & Rudy, R. J. (2005). Maui Mesosphere and lower thermosphere (Maui MALT) observations of the evolution of Kelvin-Helmholtz billows formed near 86 km altitude. *Journal of Geophysical Research*, *110*(D9), D09S10. https://doi.org/10.1029/2003JD003908

Hecht, J. H., Wan, K., Gelinas, L. J., Fritts, D. C., Walterscheid, R. L., Rudy, R. J., et al. (2014). The life cycle of instability features measured from the Andes lidar observatory over Cerro Pachon on 24 March 2012. *Journal of Geophysical Research: Atmospheres*, *119*(14), 8872–8898. https://doi.org/10.1002/2014JD021726

Hysell, D., Larsen, M., Fritts, D., Laughman, B., & Sulzer, M. (2018). Major upwelling and overturning in the mid-latitude F region ionosphere. *Nature Communications*, *9*(1), 3326. https://doi.org/10.1038/s41467-018-05809-x

Hysell, D. L., Nossa, E., Larsen, M. F., Munro, J., Smith, S., Sulzer, M. P., & González, S. A. (2012). Dynamic instability in the lower thermosphere inferred from irregular sporadic E layers. *Journal of Geophysical Research*, *117*(A8), A08305. https://doi.org/10.1029/2012JA017910

James, P. K., & Browning, K. A. (1981). An observational study of primary and secondary billows in the free atmosphere. *Quarterly Journal of the Royal Meteorological Society*, *107*(452), 357–365. https://doi.org/10.1002/qj.49710745207

Jeong, J., & Hussain, F. (1995). On the identification of a vortex. *Journal of Fluid Mechanics*, *285*, 69–94. https://doi.org/10.1017/s0022112095000462

Kelley, M. C., Chen, C. Y., Beland, R. R., Woodman, R., Chau, J. L., & Werne, J. (2005). Persistence of a Kelvin-Helmholtz instability complex in the upper troposphere. *Journal of Geophysical Research*, *110*(D14), D14106. https://doi.org/10.1029/2004JD005345

Kelvin, L. (1880). Vibrations of a columnar vortex. *Philosophical Magazine*, *10*, 155–168.

Kjellstrand, C. B., Fritts, D. C., Miller, A. D., Williams, B. P., Kaifler, N., Geach, C., et al. (2022). Multi-scale Kelvin-Helmholtz instability dynamics observed by PMC Turbo on 12 July 2018: 1. Secondary instabilities and billow interactions. *Journal of Geophysical Research*, e2021JD036232. https://doi.org/10.1029/2021JD036232

Klaassen, G. P., & Peltier, W. R. (1985). The onset of turbulence in finite-amplitude Kelvin-Helmholtz billows. *Journal of Fluid Mechanics*, *155*, 1–35. https://doi.org/10.1017/s0022112085001690

Klaassen, G. P., & Peltier, W. R. (1989). The role of transverse secondary instabilities in the evolution of free shear layers. *Journal of Fluid Mechanics*, *202*, 367–402. https://doi.org/10.1017/s0022112089001229

Klaassen, G. P., & Peltier, W. R. (1991). The influence of stratification on secondary instabilities in free shear layers in finite-amplitude Kelvin-Helmholtz billows. *Journal of Fluid Mechanics*, *227*, 71–106. https://doi.org/10.1017/s0022112091000046

Larsen, M. F. (2002). Winds and shears in the mesosphere and lower thermosphere: Results from four decades of chemical release wind measurements. *Journal of Geophysical Research*, *107*(A8), SIA28-1–SIA28-14. https://doi.org/10.1029/2001JA000218

Lehmacher, G. A., Guo, L., Kudeki, E., Reyes, P. M., Akgiray, A., & Chau, J. L. (2007). High-resolution observations of mesospheric layers with the Jicamarca VHF radar. *Advances in Space Research*, *40*(6), 734–743. https://doi.org/10.1016/j.asr.2007.05.059

Lelong, M.-P., & Dunkerton, T. J. (1998). Inertia–gravity wave breaking in three dimensions. Part I: Convectively stable waves. *Journal of the Atmospheric Sciences*, *55*(15), 2473–2488. https://doi.org/10.1175/1520-0469(1998)055<2473:igwbit>2.0.co;2

Li, F., Liu, A. Z., Swenson, G. R., Hecht, J. H., & Robinson, W. A. (2005). Observations of gravity wave breakdown into ripples associate with dynamical instabilities. *Journal of Geophysical Research*, *110*(D9), D09S11. https://doi.org/10.1029/2004JD004849

Liu, H.-L. (2021). Effective vertical diffusion by atmospheric gravity waves. *Geophysical Research Letters*, *48*(1), e2020GL091474. https://doi.org/10.1029/2020GL091474

Luce, H., Fukao, S., Dalaudier, F., & Crochet, M. (2002). Strong mixing events observed near the tropopause with the MU radar and high-resolution balloon techniques. *Journal of the Atmospheric Sciences*, *59*(20), 2885–2896. https://doi.org/10.1175/1520-0469(2002)059<2885:smeont>2.0.co;2

Luce, H., Hassenpflug, G., Yamamoto, M., Fukao, S., & Sato, K. (2008). High-resolution observations with MU radar of a KH instability triggered by an inertia-gravity wave in the upper part of a Jet-Stream. *Journal of the Atmospheric Sciences*, *65*(5), 1711–1718. https://doi.org/10.1175/2007jas2346.1

Ludlam, F. H. (1967). Billow clouds and their relation to clear air turbulence. *Quarterly Journal of the Royal Meteorological Society*, *93*(398), 419–435. https://doi.org/10.1002/qj.49709339803

Mashayek, A., & Peltier, W. R. (2012). The 'zoo' of secondary instabilities precursory to stratified shear flow transition. Part 1 Shear aligned convection, pairing, and braid instabilities. *Journal of Fluid Mechanics*, *708*, 5–44. https://doi.org/10.1017/jfm.2012.304

Mesquita, R. L. A., Larsen, M. F., Azeem, I., Stevens, M. H., Williams, B. P., Collins, R. L., & Li, J. (2020). In situ observations of neutral shear instability in the statically stable high-latitude mesosphere and lower thermosphere during quiet geomagnetic conditions. *Journal of Geophysical Research: Space Physics*, *125*(8), e2020JA027972. https://doi.org/10.1029/2020JA027972

Moin, P., & Mahesh, K. (1998). Direct numerical simulation: A tool in turbulence research. *Annual Review of Fluid Mechanics*, *30*(539), 78–578. https://doi.org/10.1146/annurev.fluid.30.1.539

Palmer, T. L., Fritts, D. C., & Andreassen, O. (1996). Evolution and breakdown of Kelvin-Helmholtz billows in stratified compressible flows, II: Instability structure, evolution, and energetics. *Journal of the Atmospheric Sciences*, *53*(22), 3192–3212. https://doi.org/10.1175/1520-0469(1996)053<3192:eabokb>2.0.co;2

Palmer, T. L., Fritts, D. C., Andreassen, O., & Lie, I. (1994). Three-dimensional evolution of Kelvin-Helmholtz billows in stratified compressible flow. *Geophysical Research Letters*, *21*(21), 2287–2290. https://doi.org/10.1029/94gl01714

Patterson, G. S., & Orszag, S. A. (1971). Spectral calculations of isotropic turbulence: Efficient removal of aliasing interactions. *Physics of Fluids*, *14*(11), 2538–2541. https://doi.org/10.1063/1.1693365

Pfrommer, T., Hickson, P., & She, C.-Y. (2009). A large-aperture sodium fluorescence lidar with very high resolution for mesopause dynamics and adaptive optics studies. *Geophysical Research Letters*, *35*(15), L15831. https://doi.org/10.1029/2009GL038802

Pope, S. B. (2000). *Turbulent flows*. Cambridge University Press. https://doi.org/10.1017/CBO9780511840531

Schowalter, D. G., Van Atta, C. W., & Lasheras, J. C. (1994). A study of streamwise vortex structure in a stratified shear flow. *Journal of Fluid Mechanics*, *281*, 247–291. https://doi.org/10.1017/s0022112094003101

Scorer, R. (1951). Billow clouds. *Quarterly Journal of the Royal Meteorological Society*, *77*(332), 235–240. https://doi.org/10.1002/qj.49707733208

Scorer, R., & Wexler, H. (1963). *A colour guide to clouds*. Pergamon Press.

Scorer, R. S. (1969). Billow mechanics. *Radio Science*, *4*(12), 1299–1307. https://doi.org/10.1029/rs004i012p01299

Smyth, W. D. (2003). Secondary Kelvin-Helmholtz instability in weakly stratified shear flow. *Journal of Fluid Mechanics*, *497*, 67–98. https://doi.org/10.1017/s0022112003006591

Smyth, W. D. (2004). Kelvin-Helmholtz billow evolution from a localized source. *The Quarterly Journal of the Royal Meteorological Society*, *130*(603), 2753–2766. https://doi.org/10.1256/qj.03.226

Thorpe, S. A. (1971). Experiments on the instability of stratified shear flows: Miscible fluids. *Journal of Fluid Mechanics*, *46*(2), 299–320. https://doi.org/10.1017/s0022112071000557

Thorpe, S. A. (1973a). Experiments on instability and turbulence in a stratified shear flow. *Journal of Fluid Mechanics*, *61*(4), 731–751. https://doi.org/10.1017/s0022112073000911

Thorpe, S. A. (1973b). Turbulence in stably stratified fluids: A review of laboratory experiments. *Boundary-Layer Meteorology*, *5*(1), 95–119. https://doi.org/10.1007/bf02188314

Thorpe, S. A. (1985). Laboratory observations of secondary structures in Kelvin-Helmholtz billows and consequences for ocean mixing. *Geophysical & Astrophysical Fluid Dynamics*, *34*(1–4), 175–199. https://doi.org/10.1080/03091928508245442

Thorpe, S. A. (1987). Transitional phenomena and the development of turbulence in stratified fluids: A review. *Journal of Geophysical Research*, *92*(C5), 5231–5248. https://doi.org/10.1029/jc092ic05p05231

Thorpe, S. A. (1999). A note on the breaking of internal waves in the ocean. *Journal of Physical Oceanography*, *29*(9), 2433–2441. https://doi.org/10.1175/1520-0485(1999)029<2433:otboiw>2.0.co;2

Thorpe, S. A. (2002). The axial coherence of Kelvin-Helmholtz billows. *Quarterly Journal of the Royal Meteorological Society*, *128*(583), 1529–1542. https://doi.org/10.1002/qj.200212858307

Thorpe, S. A. (2018). Models of energy loss from internal waves breaking in the ocean. *Journal of Fluid Mechanics*, *836*, 72–116. https://doi.org/10.1017/jfm.2017.780

Werne, J., & Fritts, D. C. (1999). Stratified shear turbulence: Evolution and statistics. *Geophysical Research Letters*, *26*(4), 439–442. https://doi.org/10.1029/1999gl900022

Williamson, J. H. (1980). Low-storage Runga-Kutta schemes. *Journal of Computational Physics*, *35*(1), 48–56. https://doi.org/10.1016/0021-9991(80)90033-9

Witt, G. (1962). Height, structure and displacements of noctilucent clouds. *Tellus*, *14*, 1–18. https://doi.org/10.1111/j.2153-3490.1962.tb00115.x

Yue, J., Nakamura, T., She, C.-Y., Weber, M., Lyons, W., & Li, T. (2010). Seasonal and local time variability of ripples from airglow imager observations in US and Japan. *Annales Geophysicae*, *28*(7), 1401–1408. https://doi.org/10.5194/angeo-28-1401-2010